Adaptive locomotion of active solids

Jonas Veenstra,[1,*] Colin Scheibner,[2,3,*] Martin Brandenbourger,[1,4,*] Jack Binysh,[1] Anton Souslov,[5] Vincenzo Vitelli,[2,3,6] and Corentin Coulais[1]

[1] *Institute of Physics, Universiteit van Amsterdam, Science Park 904, 1098 XH Amsterdam, The Netherlands*
[2] *James Franck Institute, The University of Chicago, Chicago, Illinois 60637, USA*
[3] *Department of Physics, The University of Chicago, Chicago, Illinois 60637, USA*
[4] *Aix-Marseille Université, CNRS, Centrale Méditerranée, IRPHE, UMR 7342, 13384 Marseille, France*
[5] *TCM Group, Cavendish Laboratory, JJ Thomson Avenue, Cambridge, CB3 0HE, United Kingdom*
[6] *Kadanoff Center for Theoretical Physics, The University of Chicago, Chicago, Illinois 60637, USA*

Active systems composed of energy-generating microscopic constituents are a promising platform to create autonomous functional materials [1–14] that can, for example, locomote through complex and unpredictable environments. Yet, coaxing these energy sources into useful mechanical work has proved challenging. Here, we engineer active solids based on centimetre scale building blocks that perform adaptive locomotion. These prototypes exhibit a non-variational form of elasticity characterised by odd moduli [7, 11, 15, 16] whose magnitude we predict from microscopics using coarse grained theories, and which we validate experimentally. When interacting with an external environment, these active solids spontaneously undergo limit cycles of shape-changes, which naturally lead to locomotion such as rolling and crawling. The robustness of the locomotion is rooted in an emergent feedback loop between the active solid and the environment, which is mediated by elastic deformations and stresses. As a result, our active solids are able to accelerate, adjust their gaits, and locomote through a variety of terrains with a similar performance to more complex control strategies implemented by neural networks. Our work establishes active solids as a bridge between materials, and robots and suggests decentralised strategies to control the non-linear dynamics of biological systems [7, 17–20], soft materials [4, 5, 8, 10, 11, 21–23], and driven nanomechanical devices [6, 24–28].

Nature is rife with examples of adaptive locomotion. Cells, fungi, and microorganisms autonomously move, deform, and explore their environments [29, 30], while animals run, crawl, roll and jump [31, 32]. Although robots [33–35] and active metamaterials [36–38] can mimic these behaviours, they typically struggle in unpredictable terrains, unless considerable engineering resources are employed [39]. Most robots rely on centralised feedback control: sensory signals are centrally processed before redistribution to the actuating parts. In contrast, living systems manage to robustly execute adaptive locomotion by distributing control across many scales: from autoinhibition in molecular motors [40] and mechanical sensing in cells [41] to locomotor reflexes in more complex organisms [42]. Inspired by the deep level of integration and extreme resilience of living systems, we ask: how to use purely local feedback to create synthetic materials that perform mechanical tasks as complex as adaptive locomotion?

Locomotion is often powered by cyclical shape changes that break time-reversal symmetry [43]. Our strategy to achieve adaptive locomotion through these cycles is to construct scalable building blocks with non-reciprocal interactions that generalise the familiar concept of bond-bending interactions. The building block consists of two vertices described by two bond angles θ_1 and θ_2. The torques τ_1 and τ_2 on each vertex are related to the angular displacements via

$$\begin{pmatrix}\tau_1\\ \tau_2\end{pmatrix} = \begin{pmatrix}-\kappa & -\kappa^a\\ \kappa^a & -\kappa\end{pmatrix}\begin{pmatrix}\delta\theta_1\\ \delta\theta_2\end{pmatrix} \tag{1}$$

or equivalently $\tau_i = M_{ij}\delta\theta_j$. In addition to the bond-bending stiffness κ, the matrix M_{ij} has an off-diagonal component κ^a, which represents an asymmetric coupling between the two angles. In a passive system, e.g., two pendula coupled by a spring, M_{ij} would be symmetric, according to the Maxwell-Betti reciprocity theorem [44]. Here, we remove this restriction and use programmable local feedback (see Eq. (M1) in Methods) to enable an antisymmetric (or odd) contribution in the matrix, i.e., $M_{ij} \neq M_{ji}$.

Fig. 1(a-d) illustrates the physical consequences of this oddness: for $\kappa^a > 0$ when θ_1 is decreased, θ_2 also decreases; but when θ_2 is decreased, θ_1 increases instead. We now take these non-reciprocal building blocks and build them into larger structures, both one-dimensional rings (Fig. 1e) and two-dimensional lattices (Fig. 1i). We probe the linear response of these structures by levitating them on an air table (see S.I.) and compressing them in the vertical direction (Fig. 1fj) and shearing them horizontally (Fig. 1gk). We find that the shear deformations induced by external loading are always at an angle to the applied load: these odd materials compress when sheared in one direction, but shear in the opposite direction when compressed. In other words, the two shear modes S_1 and S_2 are coupled non-reciprocally at all scales of the mate-

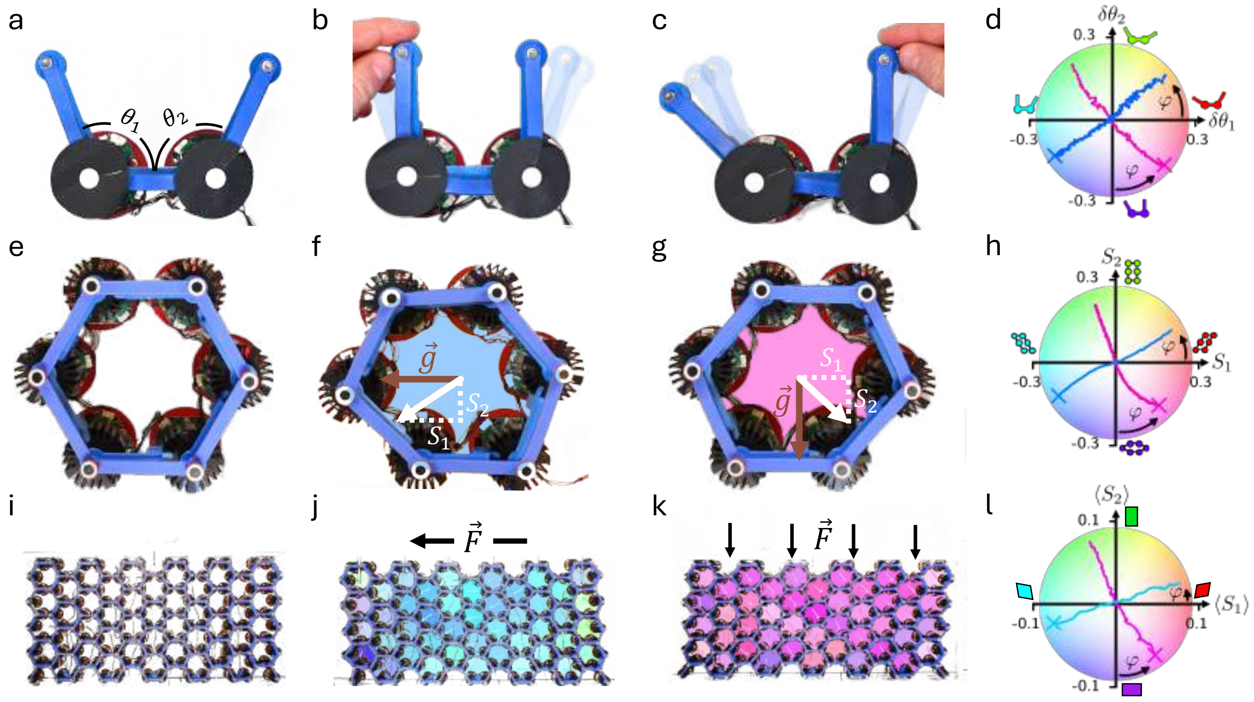

FIG. 1. **Non-reciprocal interactions induce odd responses in an active solid (a)** Three rigid linkages are connected by motorised vertices. **(b)** A hand pushes inwards on the left and the right vertex contracts. **(c)** A hand pushes inwards the right, and the left vertex expands. **(d)** Angle deviation data plotted in blue (magenta) for the left-actuated (right-actuated) building block, crosses indicate the building block's configuration as pictured in panel b (c). In a reciprocal system, the strain curves would form a cross along the two axes. Non-reciprocity rotates the strain trajectories by an angle $\varphi = \arctan(\kappa^a/\kappa)$. **(e)** Linking six vertices together forms an odd hexagon. **(f)** With its two bottom vertices held fixed, the hexagon is subjected to a gravitational body force $\vec{g}$ parallel to the hexagon's shear mode $-S_1$, leading to shear response $\vec{S}$ with a component in the $-S_2$ direction. **(g)** When gravity strains shear mode $-S_2$, the hexagon responds by extending in the positive S_1 direction. **(h)** Shear deformations of the hexagon as a result of the applied force in the S_1 direction (blue) and S_2 direction (magenta). **(i)** Tiling of 19 motorised hexagons embedded into a rectangular metamaterial consisting of 120 vertices. **(j)** When the active solid is sheared in the negative S_1 direction, the material displays a compression in the negative S_2 direction. **(k)** When the active solid is compressed in the negative S_2 direction, the material displays a shear in the positive S_1 direction. **(l)** Shear deformations of the active solid as a result of applied force in the S_1 direction (blue) and S_2 direction (magenta). See Supplemental Video 1.

rial (Fig. 1hl). In the continuum limit, this non-reciprocal response can be described by a non-variational form of elasticity called odd elasticity [16, 44]. Unlike most active solids [7, 23, 45, 46], our odd elastic metamaterials do not rely on angular (or linear) momentum sources in order to function, making them especially suitable for creating self-supporting structures.

We now show that breaking reciprocity enables our active solids to unidirectionally exchange momentum with their environment. We turn first to the most basic probe of matter, equally familiar to scientists or kids alike: smashing things into each other. In Fig. 2a, an $N = 12$-sided projectile with a positive odd stiffness $\kappa^a > 0$ is launched towards an inelastic passive surface with normal incidence. Unlike a carefully swatted tennis ball, the incoming odd projectile has no initial rotation and unlike a rugby ball, it is isotropic. Yet it deforms asymmetrically upon impact and thereby steers its outgoing trajectory to an angle determined by the sign of the κ^a (Extended Data Fig. 1. Motivated by the observation that the collision primarily excites the lowest Fourier modes of the ring, we project its deformations onto the two shear modes S_1 and S_2. Upon impact, the mode $-S_2$ compresses. Through non-reciprocal coupling, this deformation generates transverse stresses as the ring attempts to shear into its S_1 configuration. As a result of these stresses, the ring exchanges momentum with the underlying surface and is deflected horizontally. After impact, the ring's dynamics spiral through shear space towards equilibrium (Fig. 2ab): These post-impact vibrations are a manifestation of the non-Hermitian skin effect [12, 15] (see Extended Data Fig. 1 and Methods).

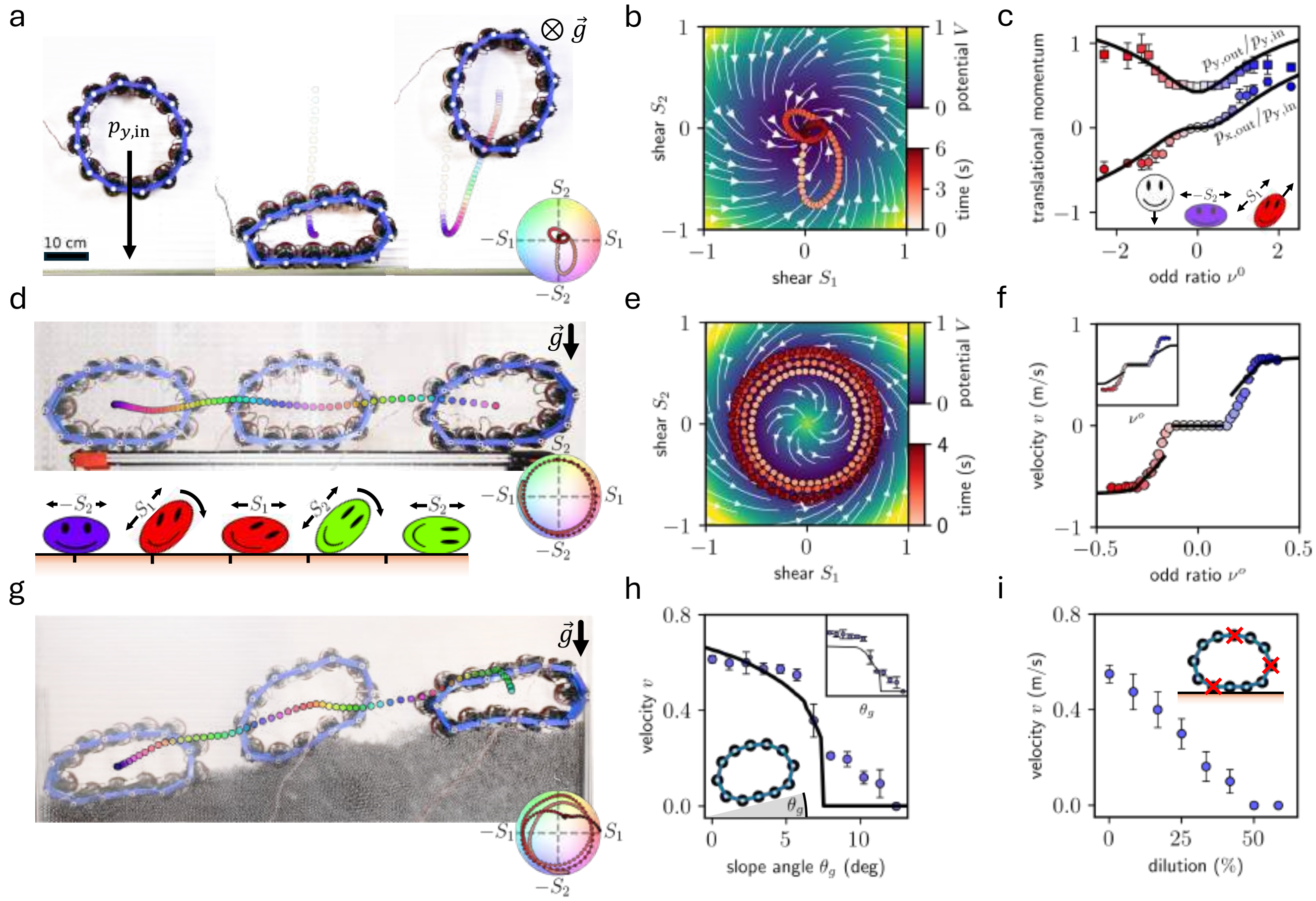

FIG. 2. **Impact deflection and locomotion of an active ring. (a)** An odd projectile with $\kappa^a > 0$ is vertically incident against a wall and rebounds under an angle. Gravity points into the page. Scale bar: 10 cm . Colormap shows the trajectory in shear space over time. **(b)** The potential (colormap) and full forcefield (white arrows) given by the minimal model of Eq. (2) in shear space with the shear space trajectory during and after impact plotted over time. **(c)** We measure the ratio between incoming and outgoing momenta $p_{\mathrm{out}}/p_{\mathrm{in}}$ in the x- (round markers) and y-directions (square markers) as a function of odd ratio ν^o. We model the projectile as a box that is only allowed to shear (see Methods) and solve numerically to find the solid line. (Inset) A mechanical interpretation of the unidirectional wave guiding the impact. Marker colors in (c,f) indicate the value of ν^o. **(d)** The ring locomotes on top of a treadmill under the influence of downwards pointing gravity. While doing so it circumscribes a steady cycle through shear space. Bottom inset shows an exaggerated picture of the locomotion mechanism: a smiley faced active solid initially compressed in the $-S_2$-mode (purple) deforms into the S_1 mode (red) under the influence of odd forces which induces a rolling motion eventually turning the smiley on its side in mode S_2 (green). **(e)** The potential (colormap) and full forcefield (white arrows) given by Eq. (3) in shear space with the ring's shear space trajectory plotted over time. **(f)** The steady state velocity of the ring as a function of the odd ratio ν^0. Black line shows numerical solution to an extension of Eq. (3) using fitted parameters (main panel) and coarse-grained experimental parameters (inset) (see Methods). The underestimation of the velocity in the latter method can be attributed to elastic and geometric nonlinearities not included in the model. **(g)** Locomotion on an uneven terrain consisting of ball bearings. **(h)** Steady state velocity as a function of the treadmill slope. Black line shows numerical solution to the minimal model of (f) using fitted parameters (main) and coarse-grained experimental parameters (inset) parameters and $\nu^o = 0.43$. **(i)** Steady state velocity as a function of the proportion of defective units in the ring. See Supplemental Video 2.

To describe the mechanism behind this asymmetric deflection, we formulate a minimal dimensionless equation of motion describing the dynamics of S_1 and S_2 in terms of the complex variable $z = S_1 + iS_2$ (see Methods):

$$\ddot{z} = -z + i\nu^o z - \Gamma \dot{z}. \tag{2}$$

Here, the first term on the right hand side denotes the passive elastic forces deriving from a simple quadratic potential (colormap in Fig. 2b) and Γ parameterises the viscous damping. Crucially, the odd ratio ν^o characterises the non-reciprocal coupling between the two shear modes: if S_2 is fixed in Eq. (2), S_1 adjusts to $\nu^o S_2$ while fixing S_1 adjusts S_2 to $-\nu^o S_1$. In the Methods we show that ν^o can be related to the microscopic interactions within the ring as $\nu^o = (8\pi/N)\kappa^a/\kappa$. While the elastic term in Eq. (2) drives the system back to equilibrium, the non-reciprocal term curls the force field and drives the system into a loop in shear space (white arrows in Fig. 2b) which is eventually dampened by dissipative forces. Remarkably, in both model and experiment the odd ratio amplifies the magnitude of the rebound (Fig. 2c, see Methods). This is in contrast to passive chiral or anisotropic solids, which can deflect asymmetrically but not amplify their rebound (Extended Data Fig. 3).

The difference with passive solids is even more dramatic when our active solids are subject to a continuous perturbation. We subject the ring to a gravitational force pointing downwards and allow it to interact with a treadmill (Fig. 2d). In the passive case $\kappa^a = 0$, the ring quickly comes to rest due to dissipative forces. However, with the odd forces turned on this compressed state is no longer an equilibrium state of the odd ring. Similarly to impact, transverse odd forces now shear the ring horizontally, displacing its centre of mass forward. However in contrast to impact, the sustained gravitational pull now prevents the ring from returning to equilibrium. Instead, gravity tips the centre of mass of the ring over its pivot point (see inset Fig. 2d), generating angular momentum. A cycle through a series of shape changes ensues whose frequency steadily increases (see Extended Data Fig. 4) which results in a rolling motion.

To understand the origin of this cycle, we extend the minimal model considered above and add a nonlinear term describing the effect of gravity,

$$\ddot{z} = -z + i\nu^o z - \Gamma\dot{z} + \frac{z}{|z|}, \tag{3}$$

where we represent the constant gravitational pressure through a unit vector $z/|z|$ that points along the instantaneous shear state of the ring. This nonlinear term turns the quadratic potential into a Mexican hat potential and removes the fixed point at the origin. Instead, a ring of shear states that minimise the potential appears corresponding to all the orientations of the compressed ring. However the non-conservative forces turn this circle of fixed points into a limit cycle (Fig. 2e), which in turn powers locomotion. The steady state limit cycle frequency is readily found to be $\omega = \nu^o/\Gamma$ (see Methods) which translates directly into a rolling velocity provided that the odd wheel does not slip along the substrate.

By turning on a treadmill while the ring accelerates a steady state velocity quickly settles which we measure for a range of ν^o (Fig. 2f). We find a threshold activity below which the ring is not able to accelerate. This apparent disagreement with the minimal model is explained by the fact that the wheel is not perfectly circular but rather has a discrete number of edges. Consequently in order to advance, the ring must overcome a small energy barrier at each vertex. We model this barrier by further adding a periodic stress $V \propto \sin\left(\frac{N}{2}\arg z\right)$ to Eq. (3), akin to the Peierls-Nabarro potential used to model sliding friction [47] (see Methods). By incorporating this barrier we find that the minimal model captures all of the central features of locomotion in our active solids, with remarkably good quantitative agreement between our locomotion experiments and model predictions based on independently calibrated parameters.

We now challenge the odd ring to locomote across an inclined granular terrain consisting of ball bearings and find the ring is able to adapt its gait to the uneven terrain (Fig. 2g). The adaptivity of the ring is explained by the ability of the ring to adjust its cycling frequency to a range of uphill slopes (Fig. 2h). In addition to the robustness to uneven terrain, our distributed feedback control strategy is also robust to failing vertices and ensures that stable locomotion persists up to a 50 % failure rate (Fig. 2i). This data suggests a compelling physical picture. The ring is able to adapt its gait, despite each vertex being unaware of its environment and its position in the world. As it rolls, the uneven terrain imprints itself into the local deformations of the ring. These deformations then induce forces that push the deformation unidirectionally along the ring while it exchanges momentum with the terrain. In turn, the ring rolls into a new deformed state and a feedback loop between the rings shape and external forcing emerges leading to surprisingly efficient accelerated uphill rolling. This ability to accelerate and adapt to rough terrains or resist failure gives our odd active solids a distinct advantage over other bio-inspired control schemes such as central pattern generators [48, 49]. In addition, this simple odd interaction performs comparably to computationally optimised controllers based on neural networks, which we observe to converge towards the local feedback rule despite having access to more degrees of freedom (Methods and Extended data Fig. 6).

So far, we have demonstrated that robotic functionalities naturally emerge in active solids with small numbers of degrees of freedom. We now show that these functionalities readily generalise to larger systems as the number of available modes increases. To this end, we return to the lattice shown in Fig. 1i, and characterise its non-reciprocal response in terms of continuum odd elasticity. The continuum odd response is encoded by an asymmetric elastic tensor relating shear strains S_1 ( ) and S_2 ( ) to their corresponding shear stresses and (see S.I.):

$$\begin{pmatrix} \\ \end{pmatrix} = 2\begin{pmatrix} -\mu & -K^o \\ K^o & -\mu \end{pmatrix}\begin{pmatrix} \\ \end{pmatrix} \tag{4}$$

where μ is the familiar shear modulus and K^o is the odd shear modulus [16]. The absence of a net angular momentum source in our metamaterials ensures that the odd bulk modulus A is zero in contrast to chiral active solids made from spinning particles [7, 11]. Through a theoret-

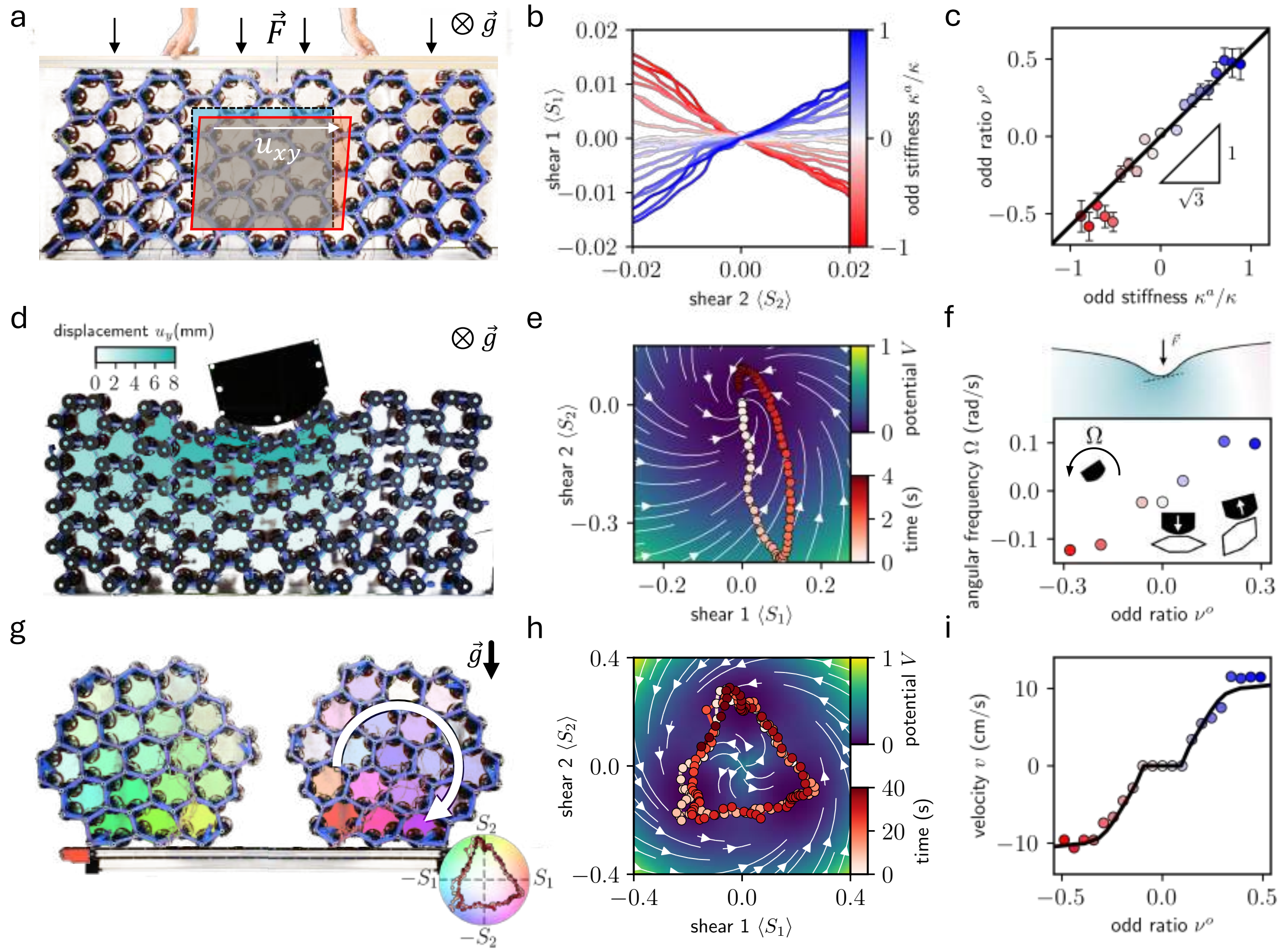

FIG. 3. **Odd elasticity, impact and locomotion in an active solid (a)** Uniaxial compression of the active metamaterial induces it to shear. **(b)** Average shear of the active solid during uniaxial compression for a range of the odd stiffness κ^a. **(c)** The odd ratio as a function of the odd stiffness, given by the slope of the shear trajectories around the equilibrium state. The solid line indicates the analytically coarse-grained prediction for the relation between microscopic interactions and continuum response (see S.I.). **(d)** A passive projectile is launched at the odd wall ($\kappa^a > 0$) and rebounds with spin, causing the wall to deform asymmetrically upon impact (see Methods). Colour represents the average vertical displacement u_y of each hexagon. **(e)** The average shear deformation in the wall with colour indicating time. **(f) (top)** Continuum solution to a point force for $\nu^o = 0.2$, echoing the asymmetric deformation of the wall observed upon impact, see Eq. (5). Colormap is that of (d). The dashed line indicates the slope at the point of contact. **(Bottom)** Measured outgoing angular frequency Ω of the impactor. (Inset lower right) The exchange of angular momentum rationalised via a single odd hexagon under impact. **(g)** A hexagonally shaped tiling of odd hexagons is placed upon the treadmill with gravity pointing downward and proceeds to roll under the effect of odd forces. Colours indicate the shear direction of each hexagon. **(h)** The average shear during internal cycles. **(i)** The steady state rolling velocity versus the odd ratio. Black line indicates numerical fit to an extension of Eq. (3) (see Methods). See Supplemental Video 3.

ical coarse-graining procedure (see S.I.) we predict that $\mu = 2\sqrt{3}\kappa/a^2$ and $K^o = 2\kappa^a/a^2$ where a denotes the vertex spacing. In Figs. 3ab we systematically vary the microscopic odd stiffness κ^a while tracking the average local shear $\langle S \rangle$ under compression, and find that the odd ratio $\nu^o \equiv \langle S_1 \rangle / \langle S_2 \rangle$ is in excellent agreement with our theoretical prediction $\nu^o = K^o/\mu = (1/\sqrt{3})\kappa^a/\kappa$ (Fig. 3c).

Having established the existence of odd elasticity in our metamaterial, we now ask how it reacts to perturbations from the environment. Mirroring our impact experiments between the odd ring and a passive surface, we launch a passive projectile at the active wall (Fig. 3d). We find that the wall responds with highly asymmetric deformations (Fig. 3de) that steer the outgoing spin of the projectile (Fig. 3f). Post-impact vibrations within the wall are then guided unidirectionally (see Extended

Data Fig. 2): This wave steering is a second manifestation of the non-Hermitian skin effect.

To intuit how the odd wall manipulates the outward trajectory of the passive projectile, we consider an idealised situation in which a point force is exerted on the boundary of the semi-infinite odd medium (Fig. 3f). In this case, the continuum solution for the vertical component of the static displacement field u_y takes the simple form (see Methods):

$$u_y = \frac{F}{2\pi\mu(1+(\nu^o)^2)}\left[2\log r + 1 - \cos 2\phi + \nu^o(\sin 2\phi + 2)\right] \tag{5}$$

where r and ϕ are polar coordinates about the point of impact and F is the applied force, which is taken to be the mass of the projectile times its deceleration. The odd ratio, ν^o in Eq. (5) introduces a term that violates the $\phi \mapsto -\phi$ symmetry. The sign of the outgoing rotational velocity Ω of the projectile can be inferred qualitatively via the S_1-S_2 shear coupling at the point of contact (Fig. 3f inset).

Next, we show that the locomotion observed in Fig. 2 is indeed a fundamental property of our active solids, independent of their precise geometry (Fig. 3g). To this end, we pack the active plaquettes into a hexagonally shaped structure and, as before, we place the structure on a treadmill under a gravitational force pointing downwards. Although the geometry, connectivity and distribution of motors are markedly different, the same mechanism responsible for locomotion in the ring configuration of Fig. 2 now orchestrates the collective rolling of the solid wheel. As the shear state of the individual hexagons is rotated around the axis of compression, the structure acquires angular momentum and starts a distinctly triangular trajectory in shear space reflecting its sixfold symmetry (Fig. 3h).

One would expect the Peierls-Nabarro potential associated to the discreteness of the structure's hexagonal shape to be larger in comparison to the twelve sided ring. However, we find that locomotion occurs at a lower oddness ν^o (Fig. 3i). We explain this puzzling effect by the presence of extra modes in the bulk causing the formation of local potential minima that decrease friction, i.e. the activation energy required to overcome the Peierl-Nabarro potential and roll.

So far, we have seen that the nonlinearity induced externally by the ground under gravity causes all parts of the odd material to enter a synchronised limit cycle which leads to accelerated rolling. However, as we now show, our active solids also host additional limit cycles as we increase the activity that power new modes of locomotion.

To observe these cycles, we return to a single building block (Fig. 4a) and increase the non-reciprocity κ^a. As the odd forces exceed the dissipative forces we observe a bifurcation. The building block becomes linearly unstable and a limit cycle sets in (Fig. 4b) with a constant magnitude beyond the threshold (Fig. 4c). This nonlinear effect is explained by the fact that the motors in our prototypes saturate at a maximum torque $\tau_{\max}$ (Fig. 4d).

We model the bifurcation by adding dissipation and inertia to the torque-angle relationship given in Eq. (1). The resulting dynamics is identical to Eq. (2), where we now interpret $z = \delta\theta_1 + i\delta\theta_2$ as the angular deflection of a single building block, Γ as the dimensionless hinge dissipation and $\nu^o = \kappa^a/\kappa$ as the non-reciprocity. In the Methods we perform a stability analysis of Eq. (1) and find a Hopf bifurcation at $\kappa^a/\kappa = \Gamma = 0.18 \pm 0.03$, in agreement with the experiment. To model post-bifurcation dynamics, we incorporate motor saturation into Eq. (2) by modifying the nonreciprocal torque-angle relationship $f(z) = i\kappa^a z$ to a piecewise linear function (black line in Fig. 4d):

$$f(z) = \begin{cases} i\kappa^a z & \text{if } |z| < \tau_{\max}/|\kappa^a| \\ i\tau_{\max}\frac{z}{|z|} & \text{if } |z| > \tau_{\max}/|\kappa^a|. \end{cases} \tag{6}$$

This saturation is a generic form of nonlinearity—other geometric or dissipative sources of nonlinearities may play a similar role in non-conservative active and biological systems [7, 50]. Solving this nonlinear extension of Eq. (2) yields a stable limit cycle, with an amplitude $z_{\lim} = \tau_{\max}/\Gamma = 0.5 \pm 0.1$ in agreement with our experiments (black line Fig. 4c). We have demonstrated a second mechanism to achieve limit cycles that emerge in the large activity regime.

We show next that this regime can be used to power crawling and achieve multimodal adaptive locomotion. We place an active chain in a constricted channel (Fig. 4e) and on top of a granular substrate (Fig. 4f) and observe a non-linear generalisation of the non-Hermitian skin effect (Fig. 4g) [12, 15] throughout the chain that exchanges momentum with the grains, propelling it forward. In this regime, the odd wheel no longer strains homogeneously as in Fig. 3g, but instead each hexagon is attracted to its own limit cycle. When placed upon the flat treadmill, the chiral nature of these excitations still move the wheel's center of mass forwards which leads to robust rolling but at a rolling frequency that does not match the internal limit cycle deformations (Fig. 4h left). When faced with inclined terrain the disordered excitations do not generate sufficient rotational momentum to overcome the energy barrier required to start rolling. However, another gait emerges as the local limit cycles at the base of the wheel now generate a crawling motion allowing it to keep moving uphill (Fig. 4h right). Although the internal deformations and overall motion of the material are much more chaotic at first sight, the trajectory through the averaged shear space $\langle S\rangle$ shows two distinct and stable limit cycles for rolling and crawling (Fig. 4i).

We have shown how bioinspired robotic functionali-

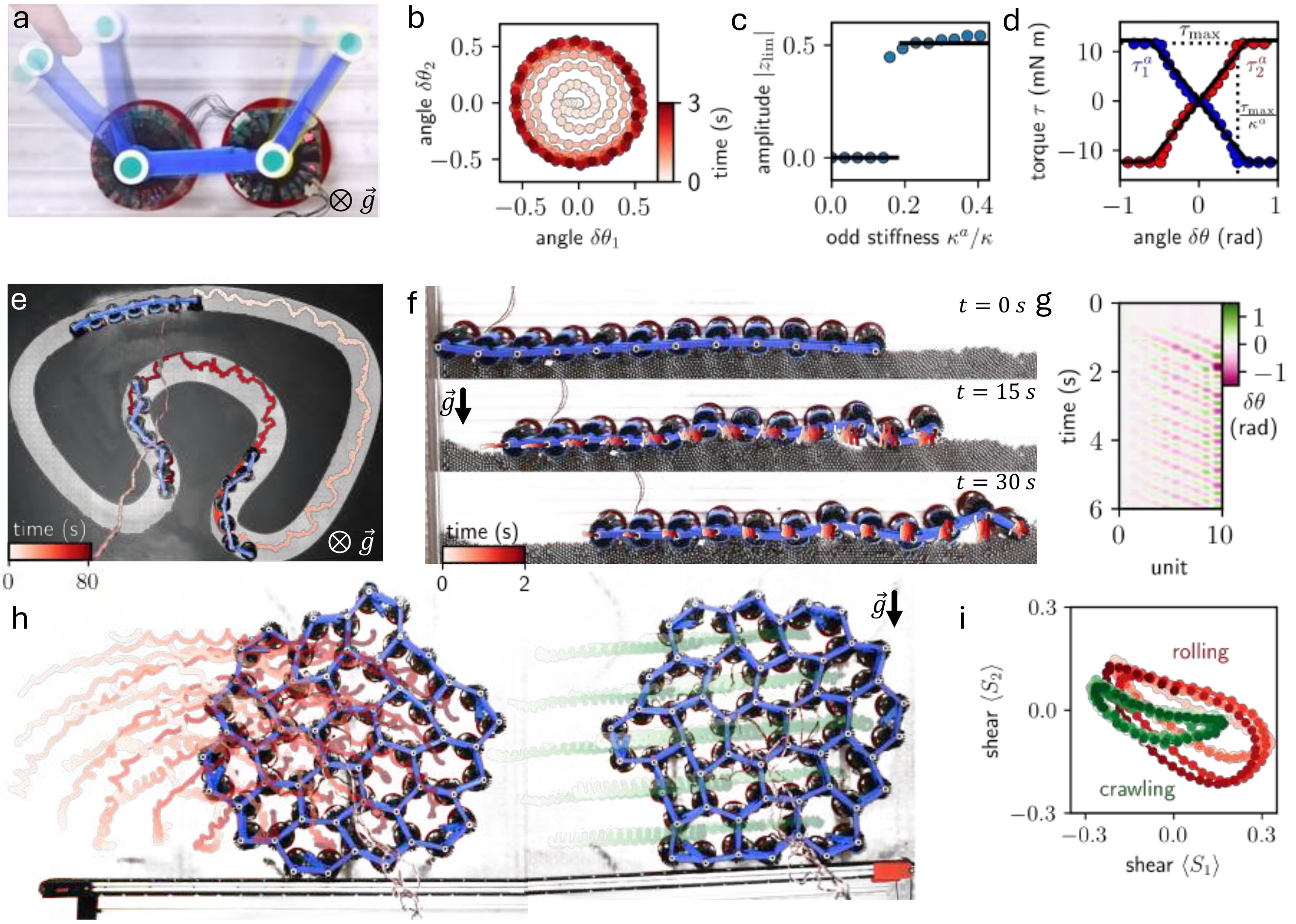

FIG. 4. **Nonlinear active solids exhibit a host of locomotion patterns.** **(a)** The odd building block exhibits stable oscillations. **(b)** Upon perturbation, deformations amplify exponentially before stabilising to a limit cycle. **(c)** When the odd stiffness exceeds the critical value of $\kappa^a/\kappa = 0.18 \pm 0.03$, a stable limit cycle emerges with an amplitude proportional the saturation torque $\tau_{\rm max}$ of the motor. **(d)** The motor torque τ^a saturates at a maximum torque $\tau_{\rm max}$ when the neighbor angle exceeds $\tau_{\rm max}/\kappa^a$. Data shown corresponds to $\kappa^a/\kappa = 0.2$. Black lines show model using experimental parameters (see Methods). **(e)** A chain of linearly unstable building blocks navigates through an irregularly shaped constriction. **(f)** Nonlinear non-Hermitian skin waves emerge in the odd chain and couple to a granular substrate with gravity pointing down, resulting in directed motion to the right. **(g)** A kymograph with the angle deviations at each vertex over time clearly shows the skin waves. **(h)** Limit cycles also emerge in the hexagonal tilings of the active solid which lead to rolling on flat terrain but induce a crawling motion when it encounters a sloped terrain. **(i)** The shear deformations during both modes of locomotion projected onto the lowest mode, showing two distinct limit cycles. See Supplemental Video 4.

ties can emerge from simple non-reciprocal interactions. Looking ahead at potential next steps in the design of animate materials [14], we envision engineering anisotropic self-standing 3D active solids that carry and manipulate loads while learning on the fly to adapt their dynamical behaviour to the environment [51].

* These authors contributed equally

[1] J. Aguilar, T. Zhang, F. Qian, M. Kingsbury, B. McInroe, N. Mazouchova, C. Li, R. Maladen, C. Gong, M. Travers, R. L. Hatton, H. Choset, P. B. Umbanhowar, and D. I. Goldman, A review on locomotion robophysics: the study of movement at the intersection of robotics, soft matter and dynamical systems, Rep. Prog. Phys. **79**, 110001 (2016).
[2] J. Aguilar, D. Monaenkova, V. Linevich, W. Savoie, B. Dutta, H. S. Kuan, M. D. Betterton, M. A. D. Goodisman, and D. I. Goldman, Collective clog control: Optimizing traffic flow in confined biological and robophysical excavation, Science **361**, 672 (2018).
[3] W. Savoie, T. A. Berrueta, Z. Jackson, A. Pervan, R. Warkentin, S. Li, T. D. Murphey, K. Wiesenfeld, and D. I. Goldman, A robot made of robots: Emergent transport and control of a smarticle ensemble, Sci. Robot. **4**

(2019).
[4] J. Palacci, S. Sacanna, A. P. Steinberg, D. J. Pine, and P. M. Chaikin, Living crystals of light-activated colloidal surfers, Science **339**, 936 (2013).
[5] A. Aubret, Q. Martinet, and J. Palacci, Metamachines of pluripotent colloids, Nat. Commun. **12**, 6398 (2021).
[6] M. Z. Miskin, A. J. Cortese, K. Dorsey, E. P. Esposito, M. F. Reynolds, Q. Liu, M. Cao, D. A. Muller, P. L. McEuen, and I. Cohen, Electronically integrated, mass-manufactured, microscopic robots, Nature **584**, 557 (2020).
[7] T. H. Tan, A. Mietke, J. Li, Y. Chen, H. Higinbotham, P. J. Foster, S. Gokhale, J. Dunkel, and N. Fakhri, Odd dynamics of living chiral crystals, Nature **607**, 287 (2022).
[8] T. Sanchez, D. T. Chen, S. J. DeCamp, M. Heymann, and Z. Dogic, Spontaneous motion in hierarchically assembled active matter, Nature **491**, 431 (2012).
[9] D. Needleman and Z. Dogic, Active matter at the interface between materials science and cell biology, Nat. Rev. Mater. **2**, 17048 (2017).
[10] A. Bricard, J. B. Caussin, N. Desreumaux, O. Dauchot, and D. Bartolo, Emergence of macroscopic directed motion in populations of motile colloids, Nature **503**, 95 (2013).
[11] E. S. Bililign, F. Balboa Usabiaga, Y. A. Ganan, A. Poncet, V. Soni, S. Magkiriadou, M. J. Shelley, D. Bartolo, and W. T. M. Irvine, Motile dislocations knead odd crystals into whorls, Nat. Phys. **18**, 212 (2022).
[12] S. Shankar, A. Souslov, M. J. Bowick, M. C. Marchetti, and V. Vitelli, Topological active matter, arXiv:2010.00364 (2020).
[13] M. C. Marchetti, J. F. Joanny, S. Ramaswamy, T. B. Liverpool, J. Prost, M. Rao, and R. A. Simha, Hydrodynamics of soft active matter, Rev. Mod. Phys. **85**, 1143 (2013).
[14] P. Ball, Animate materials, MRS Bull. **46**, 553 (2021).
[15] M. Brandenbourger, X. Locsin, E. Lerner, and C. Coulais, Non-reciprocal robotic metamaterials, Nat. Commun. **10**, 4608 (2019).
[16] C. Scheibner, A. Souslov, D. Banerjee, P. Surówka, W. T. M. Irvine, and V. Vitelli, Odd elasticity, Nat. Phys. **16**, 475 (2020).
[17] G. Peyret, R. Mueller, J. d'Alessandro, S. Begnaud, P. Marcq, R. M. Mege, J. M. Yeomans, A. Doostmohammadi, and B. Ladoux, Sustained oscillations of epithelial cell sheets, Biophys. J. **117**, 464 (2019).
[18] W. Gilpin, M. S. Bull, and M. Prakash, The multiscale physics of cilia and flagella, Nat. Rev. Phys. **2**, 74 (2020).
[19] E. Marder and D. Bucher, Central pattern generators and the control of rhythmic movements, Curr. Biol. **11**, R986 (2001).
[20] I. Lavi, M. Piel, A.-M. Lennon-Duménil, R. Voituriez, and N. S. Gov, Deterministic patterns in cell motility, Nat. Phys. **12**, 1146 (2016).
[21] F. C. Keber, E. Loiseau, T. Sanchez, S. J. DeCamp, L. Giomi, M. J. Bowick, M. C. Marchetti, Z. Dogic, and A. R. Bausch, Topology and dynamics of active nematic vesicles, Science **345**, 1135 (2014).
[22] L. Giomi and A. DeSimone, Spontaneous division and motility in active nematic droplets, Phys. Rev. Lett. **112**, 147802 (2014).
[23] P. Baconnier, D. Shohat, C. H. López, C. Coulais, V. Démery, G. Düring, and O. Dauchot, Selective and collective actuation in active solids, Nat. Phys. **18**, 1234 (2022).
[24] M. Z. Miskin, K. J. Dorsey, B. Bircan, Y. Han, D. A. Muller, P. L. McEuen, and I. Cohen, Graphene-based bimorphs for micron-sized, autonomous origami machines, Proc. Natl. Ac. Sc. U.S.A. **115**, 466 (2018).
[25] A. McDonald and A. A. Clerk, Exponentially-enhanced quantum sensing with non-hermitian lattice dynamics, Nat. Commun. **11**, 5382 (2020).
[26] J. P. Mathew, J. D. Pino, and E. Verhagen, Synthetic gauge fields for phonon transport in a nano-optomechanical system, Nat. Nanotech. **15**, 198 (2020).
[27] C. C. Wanjura, J. J. Slim, J. del Pino, M. Brunelli, E. Verhagen, and A. Nunnenkamp, Quadrature nonreciprocity in bosonic networks without breaking time-reversal symmetry, Nat. Phys. **19**, 1429 (2023).
[28] T. Liu, J.-Y. Ou, K. F. MacDonald, and N. I. Zheludev, Photonic metamaterial analogue of a continuous time crystal, Nat. Phys. **19**, 986 (2023).
[29] J. A. Nirody, L. A. Duran, D. Johnston, and D. J. Cohen, Tardigrades exhibit robust interlimb coordination across walking speeds and terrains, Proc. Natl. Acad. Sci. U. S. A. **118**, e2107289118 (2021).
[30] M. Kramar and K. Alim, Encoding memory in tube diameter hierarchy of living flow network, Proc. Natl. Acad. Sci. U. S. A. **118**, e2007815118 (2021).
[31] R. Full, K. Earls, M. Wong, and R. Caldwell, Locomotion like a wheel?, Nature **365**, 495 (1993).
[32] A. Biewener and S. Patek, *Animal Locomotion* (Oxford University Press, 2018).
[33] A. J. Ijspeert, A. Crespi, D. Ryczko, and J.-M. Cabelguen, From swimming to walking with a salamander robot driven by a spinal cord model, Science **315**, 1416 (2007).
[34] R. Thandiackal, K. Melo, L. Paez, J. Herault, T. Kano, K. Akiyama, F. Boyer, D. Ryczko, A. Ishiguro, and A. J. Ijspeert, Emergence of robust self-organized undulatory swimming based on local hydrodynamic force sensing, Sci. Robot. **6**, eabf6354 (2021).
[35] S. Choi, G. Ji, J. Park, H. Kim, J. Mun, J. H. Lee, and J. Hwangbo, Learning quadrupedal locomotion on deformable terrain, Sci. Robot. **8**, eade2256 (2023).
[36] H. Cui, D. Yao, R. Hensleigh, H. Lu, A. Calderon, Z. Xu, S. Davaria, Z. Wang, P. Mercier, P. Tarazaga, and X. R. Zheng, Design and printing of proprioceptive three-dimensional architected robotic metamaterials, Science **376**, 1287 (2022).
[37] Q. He, R. Yin, Y. Hua, W. Jiao, C. Mo, H. Shu, and J. R. Raney, A modular strategy for distributed, embodied control of electronics-free soft robots, Sci. Adv. **9**, eade9247 (2023).
[38] B. Saintyves, M. Spenko, and H. M. Jaeger, A self-organizing robotic aggregate using solid and liquid-like collective states, Sci. Robot. **9**, eadh4130 (2024).
[39] A compilation of robots falling down at the darpa robotics challenge, Https://www.youtube.com/watch?v=g0TaYhjpOfo.
[40] K. J. Verhey and J. W. Hammond, Traffic control: Regulation of kinesin motors (2009).
[41] Y. Chen, L. Ju, M. Rushdi, C. Ge, and C. Zhu, Receptor-mediated cell mechanosensing, Molecular Biology of the Cell **28**, 3134 (2017).
[42] E. P. Zehr and R. B. Stein, What functions do reflexes serve during human locomotion? (1999).

[43] E. M. Purcell, Life at low reynolds number, Am. J. Phys. **45**, 3 (1977).
[44] M. Fruchart, C. Scheibner, and V. Vitelli, Odd viscosity and odd elasticity, Annu. Rev. Condens. Matter Phys. **14**, 471 (2023).
[45] E. S. Bililign, F. Balboa Usabiaga, Y. A. Ganan, A. Poncet, V. Soni, S. Magkiriadou, M. J. Shelley, D. Bartolo, and W. T. M. Irvine, Motile dislocations knead odd crystals into whorls, Nat. Phys. **18**, 212 (2021).
[46] A. Poncet and D. Bartolo, When soft crystals defy newton's third law: Nonreciprocal mechanics and dislocation motility, Phys. Rev. Lett. **128**, 048002 (2022).
[47] O. M. Braun and Y. S. Kivshar, Nonlinear dynamics of the Frenkel–Kontorova model, Phys. Rep. **306**, 1 (1998).
[48] A. J. Ijspeert, Central pattern generators for locomotion control in animals and robots: A review, Neural Networks **21**, 642 (2008), robotics and Neuroscience.
[49] H. X. Ryu and A. D. Kuo, An optimality principle for locomotor central pattern generators, Scientific Reports **11**, 13140 (2021).
[50] M. Fruchart, R. Hanai, P. B. Littlewood, and V. Vitelli, Non-reciprocal phase transitions, Nature **592**, 363 (2021).
[51] R. Mandal, R. Huang, M. Fruchart, P. G. Moerman, S. Vaikuntanathan, A. Murugan, and V. Vitelli, Learning dynamical behaviors in physical systems, (2024), arXiv:2406.07856 [cond-mat.soft].
[52] V. M. Martinez Alvarez, J. E. Barrios Vargas, and L. E. F. Foa Torres, Non-hermitian robust edge states in one dimension: Anomalous localization and eigenspace condensation at exceptional points, Phys. Rev. B **97**, 10.1103/PhysRevB.97.121401 (2018).
[53] S. Yao and Z. Wang, Edge states and topological invariants of non-hermitian systems, Phys. Rev. Lett. **121**, 086803 (2018).
[54] A. Ghatak, M. Brandenbourger, J. van Wezel, and C. Coulais, Observation of non-hermitian topology and its bulk-edge correspondence in an active mechanical metamaterial, Proc. Natl. Ac. Sc. U. S. A. **117**, 29561 (2020).
[55] T. Helbig, T. Hofmann, S. Imhof, M. Abdelghany, T. Kiessling, L. W. Molenkamp, C. H. Lee, A. Szameit, M. Greiter, and R. Thomale, Generalized bulk–boundary correspondence in non-hermitian topolectrical circuits, Nat. Phys. **16**, 747 (2020).
[56] L. Xiao, T. Deng, K. Wang, G. Zhu, Z. Wang, W. Yi, and P. Xue, Non-hermitian bulk–boundary correspondence in quantum dynamics, Nat. Phys. **16**, 761 (2020).
[57] Y. Chen, X. Li, C. Scheibner, V. Vitelli, and G. Huang, Realization of active metamaterials with odd micropolar elasticity, Nat. Commun. **12**, 5935 (2021).
[58] C. Coulais, R. Fleury, and J. van Wezel, Topology and broken hermiticity, Nat. Phys. **17**, 9 (2020).
[59] E. J. Bergholtz, J. C. Budich, and F. K. Kunst, Exceptional topology of non-hermitian systems, Rev. Mod. Phys. **93** (2021).
[60] C. Scheibner, W. T. M. Irvine, and V. Vitelli, Non-hermitian band topology and skin modes in active elastic media, Phys. Rev. Lett. **125**, 118001 (2020).
[61] D. Zhou and J. Zhang, Non-hermitian topological metamaterials with odd elasticity, Phys. Rev. Res. **2**, 023173 (2020).
[62] L. Landau, E. Lifshitz, A. Kosevich, J. Sykes, L. Pitaevskii, and W. Reid, *Theory of Elasticity*, Course of theoretical physics (Elsevier Science, 1986).
[63] Q. Duan, G. Zhou, C. Shao, Z. Wang, M. Feng, Y. Huang, Y. Tan, Y. Yang, Q. Zhao, and Y. Shi, PyPop7: A pure-python library for population-based black-box optimization, (2022), arXiv:2212.05652 [cs.NE].
[64] I. Loshchilov, T. Glasmachers, and H.-G. Beyer, Large scale black-box optimization by limited-memory matrix adaptation, IEEE Trans. Evol. Comput. **23**, 353 (2019).
[65] C. Coulais, D. Sounas, and A. Alù, Static non-reciprocity in mechanical metamaterials, Nature **542**, 461 (2017).
[66] M. Shaat and H. S. Park, Chiral nonreciprocal elasticity and mechanical activity, J. Mech. Phys. Solids **171**, 105163 (2023).

MATERIALS AND METHODS

Construction of the robotic materials

The linkage shown in Fig. 1a is composed of motorised vertices connected by plastic arms. Each vertex consists of a DC coreless motor (Motraxx CL1628) embedded in a cylindrical heatsink, an angular encoder (CUI AMT113S), and a microcontroller (ESP32) connected to a custom electronic board. The electronic board enables power conversion, interfacing between the sensor and motor, and communication between vertices. Each vertex has a diameter 50 mm, height 90 mm, and mass 0.2 kg. The power necessary to drive the motor is provided by an external 48V DC power source.

Rigid 3D-Printed arms connect each motor's drive shaft to the heat sink of the adjacent unit. The angle formed between the two arms at vertex i is denoted by θ_i. The on-board sensor measures θ_i at a sample rate of 100 Hz and communicates the measurement to nearest neighbours. In response to the incoming signal, vertex i exerts an active torsional force τ_i^a

$$\tau_i^a = \kappa^a \left(\delta\theta_{i-1} - \delta\theta_{i+1}\right), \tag{M1}$$

where $\delta\theta_i = \theta_i - \theta^0$ and θ^0 is the rest angle (see S.I. section S5 for pseudocode). The active stiffness κ^a was programmed by the microcontroller and calibrated by measuring torque-displacement slopes for different values of the electronic feedback. The coreless motor saturates at a maximum torque of $\tau_{\max} = 12$ mN m as shown in Fig. 4d. Each link has a length of $a = 7.5$ cm. Adjacent vertices are also connected by a rubber band (blue in Fig. 1a) with a thickness 2 (4) mm which provides a passive elastic torsional stiffness of $\kappa = 20$ (48) mN m/rad used in impact (locomotion) experiments. The value of the hinge dissipation in the rubber is $\gamma = 0.4 \pm 0.1$mN m s/rad. See S.I. section S2 for calibration details.

Experimental protocol

All experiments take place on top of a custom-made low friction air table as the motors we use do not have enough torque to lift the weight of the unit cells. The table consists of two 1.5 m×1.5 m plexiglas plates that sandwich 5 mm-wide air channels. The top plate is pierced by an array of holes (pitch 10 mm, diameter 1 mm) conveying air pressurised at 10 bars. Each motorised vertex floats on a thin layer of pressurised air without making contact with the table. The experiments are filmed via a Nikon D5600 camera equipped with a 50 mm lens, recording 2 Mpx images at 50 frames per second. A marker is placed on the top of each vertex, and we use the python package OpenCV to detect and track the position of each vertex with a spatial resolution of 0.8 mm.

In Figs. 1ef, the bottom two vertices of a hexagonal structure consisting of active units are anchored while an increasing gravitational force in the indicated direction is generated by gradually tilting the air table (see Fig S4). We parameterise the internal state via the three degrees of freedom

$$S_1 = \frac{1}{\sqrt{2}}(\delta\theta_1 - \delta\theta_3) \tag{M2}$$

$$S_2 = \frac{1}{\sqrt{5}}(\delta\theta_1 + \delta\theta_3 - 2\delta\theta_5) \tag{M3}$$

$$B = \frac{1}{\sqrt{3}}(\delta\theta_1 + \delta\theta_3 + \delta\theta_5) \tag{M4}$$

The two lowest modes of an incompressible hexagon are given by the shears S_1 and S_2. The additional breathing mode B is allowed by the geometry of the hexagon but this deformation does not generate any odd forces and thus dissipates away. The projection of experimental data onto the S_1, S_2 axis is shown in Fig. 1h. In Figs. 1ijk, we perform the same experiment on a hexagonal lattice tiled in a Kekulé-O geometry (see S.I. section S3) and with sliding boundary conditions. Fig. 1l shows the average shear $\langle S \rangle$ during compression. For the 12-sided active ring in Figs. 2adg, we compute S_1 and S_2 from the real and imaginary parts of the lowest harmonic modes from the experimental data :

$$S_1(t) = -\frac{1}{6}\sum_{j=1}^{12} \cos(j\pi/3)\delta\theta_j(t) \tag{M5}$$

$$S_2(t) = \frac{1}{6}\sum_{j=1}^{12} \sin(j\pi/3)\delta\theta_j(t) \tag{M6}$$

The deformations S_1 and S_2 over time are plotted in Fig. 2be. For the 2D active material, we define the shear deformations in terms of their strains:

$$S_1 = (u_{xy} + u_{yx})/2 \tag{M7}$$

$$S_2 = (u_{yy} - u_{xx})/2 \tag{M8}$$

In Figs 3begh, $\langle S \rangle$ denotes the average shear measured over hexagons.

Impact experiments

The impact experiments shown in Fig. 2a and Fig. 3d are performed on the air table laid horizontally. In Fig. 2a, a projectile consisting of 12 active vertices is launched towards an aluminium profile. Two initial velocities of 0.26 m/s and 0.34 m/s were used with the resulting outward momentum depending only weakly on the initial velocity, (see Extended Data Fig.1) so that we chose to show the average of the observed momenta in Fig 2c. In Fig. 3f, a projectile of mass 8.2 kg was propelled towards an active hexagonal lattice of vertices with an incident velocity of 0.45 m/s. The bottom row of the wall was anchored to the aluminium profile to prevent slipping. For all impact experiments, the incoming projectile velocity was set by an aluminium profile connected to a conveyor belt and a stepper motor (Beckhoff AM8112 and controller EL7211-9014).

Locomotion experiments

In Figs. 1fg, 2dg, Fig. 3g and Figs. 4fh, the air table was tilted by 6° with respect to the horizontal plane. This creates an effective gravitational constant of $g_{\text{eff}} \approx 1\,\mathrm{m\,s^{-2}}$ that points towards a treadmill (Fig. 2d, Fig. 2g, Fig. 3g, Fig. 4h) or a granular terrain consisting of a single layer of ball bearings (Fig. 2g, Fig. 4f). The pressure resulting from the gravitational and normal forces acting upon the active solid induce odd forces that lead to an accelerating rolling motion. To prevent collision with the edges of the airtable, the treadmill is manually controlled until a steady state settles, at which point the active solid's internal deformations are measured over time. The angular frequency ω is then the slope of a linear fit of the accumulated phase $\arg z$ over time. The steady state velocity of Figs. 2fhi and Fig. 3i is then found by multiplying the angular velocity by the circumference of the solid, as slipping is observed to be negligible during rolling. For Fig 2h, we rotate the treadmill about the normal of the table at a range of angles and repeat the protocol above.

Static compression experiments

In Figs. 3a-c, we probe quantitatively the continuum response of the active solid to uniaxial compression by measuring the ratio between the two averaged shear strains $\langle S_1\rangle$ and $\langle S_2\rangle$, found by analysis of the tracking data. We use an aluminium bar with a steel wire attached to both ends and strung along the inside of the top row of units as pictured in Fig 3a to allow sliding during manual compression and extension of the material. Repeating the experiment for a range of the odd stiffness κ^a yields the shear strain curves shown in Fig 3b. We measure $\langle S_1\rangle$ and $\langle S_2\rangle$ and extract the slope $\frac{\partial\langle S_1\rangle}{\partial\langle S_2\rangle}$ around the reference state $\langle S_1\rangle = \langle S_2\rangle = 0$ to find the odd ratio ν^o for each value of κ^a, as shown in Fig. 3c. The black line is the analyical prediction of $\nu^o = \kappa^a/\sqrt{3}\kappa$, found by a coarse-graining the Kekulé geometry (see Fig. S5)). We perform numerical simulations of the active solid and find a perfect match to the experimental results (see Fig. S3)).

Linear and nonlinear dynamics of odd elastic media

Here we detail the analysis of our active solids under impact and during locomotion. For impact experiments, a linear analysis suffices to capture their observed centre of mass motion and post impact internal deformations. We then take into account nonlinearities caused by the prolonged contact with the environment during locomotion and use a nonlinear extension of our impact model to explain the observed rolling behavior over sloped terrain.

Linearised dynamics of the active solid

We observe that both impact and locomotion primarily excite the lowest Fourier modes of our active solids. As such we construct a phenomenological model that treats the solid as a block, and only tracks the two homogeneous shear modes, S_1 and S_2. The dynamics of these lowest modes can be described as a damped oscillator, with non-reciprocal interactions at the unit cell level resulting in an antisymmetric coupling between S_1 and S_2:

$$\begin{aligned} M\ddot{S}_1 &= -\mu S_1 - K^o S_2 - \eta\dot{S}_1, \\ M\ddot{S}_2 &= -\mu S_2 + K^o S_1 - \eta\dot{S}_2, \end{aligned} \tag{M9}$$

where M is the mass of the disk, μ and K^o are the shear and odd moduli, and η is the viscosity.

Writing the shear modes as a complex variable $z = S_1 + iS_2$ for compactness and non-dimensionalising time by $t \to \sqrt{M/\mu}t$, we recover Eq. (2) of the main text,

$$\ddot{z} = -z + i\nu^o z - \Gamma\dot{z}, \tag{M10}$$

with non-dimensional parameters the odd ratio $\nu^o = K^o/\mu$, and viscosity $\Gamma = \eta/\sqrt{\mu M}$. Using the ansatz $z \propto e^{-i\omega t}$ in Eq. (M10) we find a dispersion

$$\omega = -i\frac{\Gamma}{2} \pm \sqrt{-\left(\frac{\Gamma}{2}\right)^2 + (1 - i\nu^o)}. \tag{M11}$$

We now connect the effective dimensionless parameters ν^o and Γ of Eq. (M10) to the microscopic parameters of the active chain of Fig. 2, namely microscale stiffness κ and non-reciprocity κ^a, hinge dissipation γ, unit mass m, number of units N and the vertex spacing a. To do so we equate the dispersion of Eq. (M11) to the dispersion corresponding to a wave equation describing an active chain, found by a coarse-graining procedure as detailed in S.I. section S1:

$$(\partial_\tau^2 + \partial_\lambda^4 + 2\tilde{\kappa}^a\partial_\lambda^5 + \tilde{\Gamma}\partial_\lambda^4\partial_\tau)h(\lambda,\tau) = 0, \tag{M12}$$

where $h(\lambda,\tau)$ is the amplitude of the chain's deflection as a function of non-dimensional time τ and space λ, while $\tilde{\Gamma}$ is the dissipation, $\tilde{\kappa}^a = \kappa^a/N\kappa$, and N is the number of unit cells. For the lowest vibrational mode of the chain and small hinge dissipation, the dispersion is given by

$$\tilde{\omega} \propto \ -\frac{(4\pi)^2 i\gamma}{2N^2 a\sqrt{\kappa m}} \pm \sqrt{1 - i\frac{8\pi i\kappa^a}{N\kappa}}. \tag{M13}$$

Since one cycle in shear space should correspond to one cycle in the vibration of the chain, we equate $\mathrm{Re}(\omega)/\,\mathrm{Im}(\omega) = \mathrm{Re}(\tilde{\omega})/\,\mathrm{Im}(\tilde{\omega})$, and obtain

$$\nu^o = \frac{8\pi\kappa^a}{N\kappa}, \tag{M14}$$

$$\Gamma = \frac{8\pi^2\gamma}{N^2 a\sqrt{\kappa m}}. \tag{M15}$$

In terms of the dimensional quantities in Eq. (M9) the map between disk and chain parameters is given by

$$M = Nm, \tag{M16}$$

$$\mu = \frac{(4\pi)^4\kappa}{N^3a^2}, \tag{M17}$$

$$\eta = \frac{(4\pi)^4\gamma}{N^3a^2}, \tag{M18}$$

$$K^o = 2\frac{(4\pi)^5\kappa^a}{N^4a^2}. \tag{M19}$$

The dispersion of Eq. (M11) has an imaginary part with a sign that depends on the balance between ν^o and Γ. In the regime that $|\nu^o| < \Gamma$, an initial perturbation oscillates between the two shear modes and decays exponentially towards equilibrium. When $|\nu^o| > \Gamma$, ω acquires a positive imaginary component, which signals the onset of instability requiring a nonlinear analysis. In the singular case that $|\nu^o| = \Gamma$, ω is purely real and the shear trajectory will be a periodic orbit. However, this solution is experimentally inaccessible as any perturbation destabilises these orbits.

Projectile center of mass motion

To capture the center of mass motion of the projectile shown in Fig 2(a), we now equate the force on the center of mass of the block to the shear stress along the bottom surface:

$$\begin{pmatrix} F_x \\ F_y \end{pmatrix} = \alpha_1 \begin{pmatrix} \sigma_{xy} \\ \sigma_{yy} \end{pmatrix} = \begin{pmatrix} \ddot{S}_2 \\ -\ddot{S}_1 \end{pmatrix} \tag{M20}$$

where α_1 is a proportionality constant. If we denote the center of mass of the block by (x, y), then we have $S_1 = -2y/R$ and $S_2 = 2x/R$. Since the damping term in Eq. (M9) does not couple shear modes, we chose to model the dissipative losses as a prefactor Σ so that Eq. (M10) reduces to:

$$\begin{pmatrix} \ddot{x} \\ \ddot{y} \end{pmatrix} = \frac{2\mu}{ML} \begin{pmatrix} -1 & -\nu^o \\ \nu^o & -1 \end{pmatrix} \begin{pmatrix} x \\ y \end{pmatrix} \tag{M21}$$

where M is the mass of the block.

In Fig. 2c, we plot the ratios $p_{y,\mathrm{out}}/p_{y,\mathrm{in}}$ and $p_{x,\mathrm{out}}/p_{y,\mathrm{in}}$ for the simple box model. These quantities are defined as follows. We integrate Eq. (M21) using as initial conditions $(x, y) = 0$ and $\dot{y} = p_{y,\mathrm{in}}/(M\Sigma)$. We then terminate the integration when $y = 0$ (meaning that that block is departing the floor) and define the outgoing momentum $(p_{x,\mathrm{out}}, p_{y,\mathrm{out}})$. Since Eq. (M21) is linear, the quantities $(p_{x,\mathrm{out}}/p_{y,\mathrm{in}}, p_{y,\mathrm{out}}/p_{y,\mathrm{in}})$ are independent of the numerical prefactors and only depend on the value of ν^o and Σ. The value of $(p_{x,\mathrm{out}}/p_{y,\mathrm{in}}, p_{y,\mathrm{out}}/p_{y,\mathrm{in}})$ is easily determined numerically for values of the odd ratio ν^o. For small ν^o, one can also write the leading order expression:

$$\frac{p_{y,\mathrm{out}}}{p_{y,\mathrm{in}}} = \Sigma + \mathcal{O}\big(\nu^{o2}\big), \tag{M22}$$

$$\frac{p_{x,\mathrm{out}}}{p_{y,\mathrm{in}}} = \Sigma\nu^o + \mathcal{O}\big(\nu^{o2}\big). \tag{M23}$$

To compare to experiments, the value of Σ can be determined by setting the ratio of $p_{y,\mathrm{out}}/p_{y,\mathrm{in}}$ at $\nu^o = 0$. By examining the rebound at $\nu^o = 0$, we find $\Sigma = 0.42$. The theoretical predictions of Eq. (M23) are then compared against experimental measurements in Fig. 2k. Here, the markers indicate averages over all runs of the experiment and the error-bars indicate the full range.

Non-Hermitian skin waves

When $\kappa^a = 0$, Eq. (M12) is the wave equation for a thin beam with bending stiffness and dissipation. Crucially, for $\kappa^a \neq 0$, a new term $\tilde{\kappa}^a\partial_\lambda^5 h$ is introduced that violates parity symmetry $\lambda \to -\lambda$. The broken parity and Hermiticity imply that flexural waves will be amplified in one direction relative to the other, an effect known as the non-Hermitian skin effect [12, 15, 52–61]. A distinctive feature of the non-Hermitian skin effect is the strong dependence of wave spectra on boundary conditions. In the post-impact vibrations of the periodic ring shown in Extended Data Fig. 1 this effect is manifest in the unidirectional propagation and unbounded growth of linear waves. By contrast, in the open chain shown in Fig. 4efg modes remain bounded in amplitude, but localise to one edge of the chain [15] resulting in a crawling motion due to momentum exchange of the chain with its environment.

In the 2D metamaterial shown in Fig. 3d broken parity symmetry manifests as the one-way amplification of surface Rayleigh waves. In Extended Data Fig. 2 we quantify the asymmetry of wave propagation in the odd wall by measuring the center of vibration ℓ,

$$\ell = \frac{\langle x\,\hat{V}_t[u_y(\mathbf{x},t)]\rangle_{\mathbf{x}}}{\langle \hat{V}_t[u_y(\mathbf{x},t)]\rangle_{\mathbf{x}}}, \tag{M24}$$

where the variance $\hat{V}$ is over time and the average is over space. When $\nu^o = 0$, $\ell = 0$. By contrast, when $\nu^o > 0$ (< 0) the centre of vibration shifts, $\ell < 0$ (> 0). To rationalise this dependence of ℓ on ν^o, we show in S.I. section S1 that a half-infinite elastic continuum with $\nu^o \neq 0$ hosts unidirectionally amplified Rayleigh waves. Crucially, when the odd ratio $\nu^o \neq 0$, these waves acquires a nonzero exponential amplification along the boundary, quantified by an inverse growth length q_x, such that $u_y(x) \propto e^{q_x x}$.

Nonlinear dynamics originating from interactions with the environment

The ring of Fig. 2 and the 2D lattice of Fig. 3 are initially compressed by a combination of gravity and the normal force from the treadmill. With non-reciprocity turned on, active torques induce a rolling motion during which the internal deformations cycle in shear space. Here, we derive the steady state centre of mass velocity of the ring by modelling it as a disk whose only modes of deformation are S_1 and S_2.

Minimal model

We model the inertial dynamics of the shear modes $z = S_1 + iS_2$ during locomotion with a nonlinear version of Eq. (2),

$$M\ddot{z} = -\mu z + f(z) - \eta\dot{z} + g\frac{z}{|z|}\exp(2i\theta_g) + iD\frac{z}{|z|}\sin\left(\frac{N}{2}\arg z\right). \tag{M25}$$

The internal pressure field caused by gravity is parameterised by g and points in the direction of the instantaneous shear state in the case of flat terrain ($\theta_g = 0$). For an inclined terrain, the gravitational pressure is at an angle $2\theta_g$ with the orientation $\arg(z)$ of the instantaneous shear state. To account for the discrete nature of our active solids we include a potential term of strength D that is periodic in the shear cycle $\arg(z)$ with a periodicity proportional to the number of edges N of the ring ($N = 12$) or 2D solid ($N = 6$). Since one rotation of the ring corresponds to two full shear cycles, we find a period of $N/2$. Lastly, we model the odd stresses as a nonlinear function:

$$f(z) = \begin{cases} iK^o z & \text{if } |z| < \tau_{\max}/|K^o| \\ i\tau_{\max}\frac{z}{|z|} & \text{if } |z| > \tau_{\max}/|K^o|, \end{cases} \tag{M26}$$

where K^o is the odd modulus and $\tau_{\max}$ is the value of the odd stress at which the motors saturate. We start by considering locomotion on flat terrain ($\theta_g = 0$) in the regime where the odd stresses do not saturate ($|K^o| < \tau_{\max}/|z|$) and without discrete effects ($D = 0$), such that Eq. (M25) reduces to

$$M\ddot{z} = -\mu z + iK^o z - \eta\dot{z} + g\frac{z}{|z|}, \tag{M27}$$

which is equivalent to Eq. (3) under a rescaling of time $t \to \sqrt{M/\mu}t$ and shear $z \to \frac{g}{\mu}z$ and using non-dimensional parameters $\nu^o = K^o/\mu$ and $\Gamma = \eta/\sqrt{M\mu}$. In its passive state with $\nu^o = 0$, we look for equilibrium states of the solid by setting $\ddot{z} = \dot{z} = 0$ and find solutions corresponding to all the compressed shear states with magnitude $|z| = 1$ differing by a rotation $\theta = \arg z$. For nonzero odd ratio ν^o, no such static solutions exist and we instead look for cycles of constant magnitude. Switching to polar coordinates $z = Ae^{i\theta}$, we find steady state solutions by setting $\ddot{A} = \dot{A} = \ddot{\theta} = 0$ which yields a steady state frequency ω_{ss} and amplitude A_{ss},

$$\omega_{\text{ss}} = \frac{\nu^o}{\Gamma}, \tag{M28}$$

$$A_{\text{ss}} = \frac{1}{1 - \left(\frac{\nu^o}{\Gamma}\right)^2}. \tag{M29}$$

For a nonzero slope $\theta_g \neq 0$, we find the general expressions

$$\omega_{\text{ss}} = \frac{1}{\Gamma}\left(\nu^o + \frac{\sin\theta_g}{A_{\text{ss}}}\right), \tag{M30}$$

$$A_{\text{ss}} = \frac{1}{2(\Gamma^2 - \nu^{o2})}\Big[\Gamma^2\cos\theta_g + 2\nu^o\sin\theta_g + \Gamma\sqrt{\Gamma^2\cos^2\theta_g + 4\sin\theta_g(\nu^o\cos\theta_g + \sin\theta_g)}\Big]. \tag{M31}$$

When the motors saturate according to Eq. (M26), repeating the above analysis shows that the steady state frequency becomes dependent only on the sign of the odd ratio ν^o and saturates:

$$\omega_{\text{ss}} = \text{sgn}(\nu^o)\frac{\tau_{\max}}{\kappa\Gamma}. \tag{M32}$$

The limit cycle solutions are characterised by a balance between energy injection and dissipation, which only occurs at the steady state amplitude. Equation (3) can be rewritten in the form of a power balance,

$$\frac{1}{2}\frac{d}{dt}(|z|^2 + |\dot{z}|^2 - |z|) = -\Gamma|\dot{z}|^2 + \nu^o\text{Im}(z^*\dot{z}). \tag{M33}$$

The left-hand-side of Eq. (M33) gives the time derivative of the kinetic and potential energy. The right-hand-side gives the power dissipated $P_{\text{dissipated}}$ ($\sim \Gamma$) and injected P_{injected} ($\sim \nu^o$) from the non-reciprocal coupling. Inserting the limit cycle solution $z_{\text{ss}} = A_{\text{ss}}e^{i\omega_{\text{ss}}t}$ into Eq. (M33) we have that $|z| = |\dot{z}| =$ constant, and a balance between dissipation and injection at $P_{\text{injected}} = -P_{\text{dissipated}} = \nu^{o2}/\Gamma$. To find the steady state locomotion velocity, we multiply the shear cycle frequency ω_{ss} by the perimeter d of the active solid and divide by two to account for the fact that two shear cycles correspond to one global rotation of the active solid:

$$v_{\text{ss}} = \frac{\omega_{\text{ss}} d}{2}. \tag{M34}$$

In the case of the ring $d = 12a$ while for the 2D solid we use $d = 30a$. The steady state solutions to Eq. (3) suggest that locomotion occurs without threshold at any finite value of the odd ratio ν^o. However, the discreteness of our prototypes means that not all orientations of the compressed ring minimise the potential energy. We capture this effect with a periodic potential of amplitude D corresponding to the energy barrier between equilibrium configurations separated by an angle $2\pi/N$. To make contact with the experimental data, we numerically integrate Eq. (M25) using parameters $m = 2.4$ kg, $\mu = 130$ N/m, and $\eta = 10$ N/m·s found by coarse-graining calibrated experimental parameters via Eqs. (M16)- (M19). We infer the gravitational pressure $g = 54$ N/m from the rings initial amplitude $A_0 = g/\mu$ and fit the remaining phenomenological parameters $\tau_{\max} = 100$ N/m, $D = 30$ N/m to the data of Figs 2fh, yielding the black line shown in the inset of Figs 2fh. For the black line in the main panels of Figs 2fh, we use fitted parameters $m = 2.4$ kg, $\mu = 400$ N/m, $\eta = 18$ N/m·s, $g = 160$ N/m, $\tau_{\max} = 100$ N/m and $D = 100$ N/m. The black line of Fig 3i uses $M = Nm = 10.8$ kg, $\mu = 2\sqrt{3}\kappa/a^2 = 78$ N/m and fitted parameters $\eta = 259$ N/m·s, $\tau_{\max} = 5.2$ N/m, $D = 1.6$ N/m. The potential and forcefields of Fig. 2be and Fig. 3eh are calculated using the fitted parameters and the magnitude of the potential is normalised to unity.

Dynamics originating from internal nonlinearities

In Figure 4, we demonstrate robotic functionalities emerging from limit cycles at the level of a single unit cell. The building block of Fig 4a, consisting of two motorised hinges, is characterised by Eq. (1) in the static limit to linear order. However, the linkage undergoes an instability in the dynamic regime when the odd stiffness κ^a crosses a threshold value. The dynamics is captured by Eq. (M25) with $g = D = 0$, where $z = \delta\theta_1 + i\delta\theta_2$ now describes the two angular deviations of the linkage:

$$I\ddot{z} = -\kappa z + f(z) - \gamma \dot{z} \tag{M35}$$

where I is the moment of inertia of a single linkage, γ is the viscous dissipation of the hinge, and f models the saturating torques generated by the actuators in analogy to Eq. (M26):

$$f(z) = \begin{cases} i\kappa^a z & \text{if } |z| < \tau_{\max}/|\kappa^a| \\ i\tau_{\max}\frac{z}{|z|} & \text{if } |z| > \tau_{\max}/|\kappa^a|. \end{cases} \tag{M36}$$

The dimensionless parameter $\xi = \kappa^a/\gamma\sqrt{I/\kappa}$ captures the ratio of drive (κ^a) and inertia (I) to dissipation (γ) and restoring forces (κ). When $|\xi| < 1$, dissipation and restoring forces win and the process terminates at its rest configuration $z = 0$. When $|\xi| > 1$, a Hopf bifurcation occurs and a cycle emerges of finite amplitude $z_{\text{lim}} = \tau_{\max}/\gamma\sqrt{I/\kappa}$, stabilised by the saturating term $f(z)$. Using the ansatz $z = z_{\text{lim}} e^{-i\omega t}$, we obtain a solution for the amplitude $|z_{\text{lim}}|$:

$$|z_{\text{lim}}| = \frac{i\tau_{\max}}{-I\omega^2 + \kappa - i\gamma\omega}. \tag{M37}$$

The constraint that $|z_{\text{lim}}|$ must be positive and real restricts the allowed frequencies to $\omega = -\sqrt{\kappa/I}$. The full solution is given by

$$\delta\theta_1 + i\delta\theta_2 = \frac{\tau_{\max}}{\gamma}\sqrt{\frac{I}{\kappa}}\left[\cos\left(\sqrt{\frac{\kappa}{I}}t\right) + i\sin\left(\sqrt{\frac{\kappa}{I}}t\right)\right] \tag{M38}$$

up to an arbitrary phase. The black line in Fig. 4c corresponds to the values of z_{lim} and ξ found using experimental parameters $\kappa = 48 \pm 5$ mN m s/rad, $I = 10 \pm 2 \cdot 10^{-5}$ kg m^2, $\gamma = 0.4 \pm 0.1$ mN m/rad and the maximum torque was set to be $\tau_{\max} = 4 \pm 1$mN m.

Odd elasticity and response to a point force

In Fig. 3d, we measure the local displacement field u_i of each node upon impact. The colormap overlaying the reconstruction shows u_y averaged over each hexagon. For Panel e, we compute the strain tensor $u_{ij} = \frac{1}{2}(\partial_i u_j + \partial_j u_i)$ from the displacement field and average over all space. We derive here a point response an odd elastic solid given by Eq. (5), as shown in Fig. 3f and use it to model the effect of impact on the wall. On the basis of angular momentum conservation, C_3 symmetry, and isotropy, one can deduce that the elastic modulus tensor C_{ijkl} defining the stress-strain relationship in our active solids takes the following form [16]:

$$C_{ijkl} = B\delta_{ij}\delta_{kl} + \mu(\delta_{il}\delta_{jk} + \delta_{ik}\delta_{jl} - \delta_{ij}\delta_{kl}) + K^o E_{ijkl}, \tag{M39}$$

where $E_{ijkl} = \frac{1}{2}[\epsilon_{il}\delta_{jk} + \epsilon_{ik}\delta_{jl} + \epsilon_{jl}\delta_{ik} + \epsilon_{jk}\delta_{il}]$ and where δ_{ij} and ϵ_{ij} are the Kronecker and Levi-Civita symbols, respectively. Here B and μ are the well known bulk and shear moduli, while the parameter K^o is the isotropic *odd elastic* modulus. It is useful to cast Eq.(M39) into an overall stiffness E, known as the Young's modulus, as well as two dimensionless parameters: the Poisson's ratio ν and the so-called odd ratio ν^o. These parameters are given by

$$E = \frac{4B[\mu^2 + (K^o)^2]}{\mu(\mu + B) + (K^o)^2} \to 4\mu\left[1 + \left(\frac{K^o}{\mu}\right)^2\right] \quad \text{(M40)}$$

$$\nu = \frac{\mu(B - \mu) - (K^o)^2}{\mu(B + \mu) + (K^o)^2} \to 1 \quad \text{(M41)}$$

$$\nu^o = \frac{BK^o}{\mu(B + \mu) + (K^o)^2} \to \frac{K^o}{\mu}. \quad \text{(M42)}$$

The honeycomb lattice is approximately incompressible (to linear order). Hence in Eqs. (M40-M42), we show the limiting expressions as $B \to \infty$. To compute the response to a point force, we must solve the bulk equation for static equilibrium $\partial_i \sigma_{ij} = 0$. To do so, it is useful to introduce the airy stress function χ defined via $\sigma_{ij} = \epsilon_{il}\epsilon_{jk}\partial_l\partial_k\chi$. Then $\partial_i\sigma_{ij} = 0$ becomes $\Delta^2\chi = 0$. We consider a point force of magnitude F on the boundary of a semi-infinite medium with stress free boundaries. Then the airy stress function is given by [62]

$$\chi = -\frac{F}{\pi} r\phi\cos\phi, \quad \text{(M43)}$$

where ϕ is the angle with respect to the direction of the applied force. The corresponding stress is $\sigma_{rr} = -\frac{2F}{\pi r}\cos\phi$ and $\sigma_{r\phi} = \sigma_{\phi\phi} = 0$. The strain is obtained by inverting Eq. (M39):

$$u_{ij} = \frac{1}{E}\Big\{(1-\nu)\delta_{ij}\delta_{mn} + (1+\nu)(\delta_{im}\delta_{jn} + \delta_{in}\delta_{jm} - \delta_{ij}\delta_{mn}) - 2\nu^o E_{ijmn}\Big\}\sigma_{mn}. \quad \text{(M44)}$$

Eq. (M44) yields the differential equations:

$$u_{rr} = \partial_r u_r = -\frac{4F}{\pi E r}\cos\phi \quad \text{(M45)}$$

$$u_{\phi\phi} = \frac{1}{r}\partial_\phi u_\phi + \frac{u_r}{r} = \nu\frac{4F}{\pi E r}\cos\phi \quad \text{(M46)}$$

$$2u_{r\phi} = \partial_r u_\phi - \frac{u_\phi}{r} + \frac{1}{r}\partial_\phi u_r = -\nu^o\frac{8F}{\pi E r}\cos\phi. \quad \text{(M47)}$$

Solving these equations and taking the incompressible limit with $\nu = 1$, yields

$$u_r = \frac{F}{2\pi\mu(1 + (\nu^o)^2)}[-\log r\cos\phi - \nu^o(\sin\phi + \phi\cos\phi)] \quad \text{(M48)}$$

$$u_\phi = \frac{F}{2\pi\mu(1 + (\nu^o)^2)}[(1 + \log r)\sin\phi + \nu^o\phi\sin\phi]. \quad \text{(M49)}$$

The y-component of displacement is given by $u_y = -u_r\cos\phi + u_\phi\sin\phi$ yielding Eq. (5) of the main text.

Coarse-graining theory

To predict μ and K^o in Eq. (4) for the lattice shown in Fig. 3, we follow the coarse-graining procedure outlined in [16]. We first construct the reciprocal space dynamical matrix $D(\mathbf{q})$ for a ball-spring model of the lattice shown in Fig. 3. Next, we expand $D(\mathbf{q})$ in the long wavelength limit, assuming internal degrees-of-freedom relax much faster that long-wavelength modes. Finally, we read off elastic moduli from this reduced-order $D(\mathbf{q})$ (See S.I. section S4 for details).

Benchmark of odd elasticity vs. computational optimization for locomotion

Here we describe the protocol used to benchmark the locomotion performance of the local and linear feedback strategy outlined in the Main text to (1) long range feedback and (2) a neural network, both optimised on numerical simulations of the active 12 vertex ring of Fig. 2 (see SI Section 5 for details). Starting the ring from static initial conditions, we use as a metric for performance the distance travelled on a set of 200 complex terrains after a set time of $t_\mathrm{f} = 500$. We use a Python implementation [63] of the evolutionary strategy LMMA-ES [64] to optimise (1) the entries of the dynamical matrix K and (2) the weights and biases of a multilayer perceptron with dimensions $(12, 20, 1)$ using the ReLU activation function. Both sets of parameters connect input vertex angle deviations $\delta\theta_i$ to output actuation torques τ_i. Analogous to the experiment, we assume translational symmetry along the ring and let the motors saturate at a maximum torque τ_max. We verify the robustness of the learned control on a validation set of complex terrains and find that local feedback performance falls within 10% of the performance of the optimised neural network controller. Both the optimal dynamical matrix and the optimised network converge towards the local coupling considered in the main text as shown in Extended Data Fig. 6.

Acknowledgments.
We thank Daan Giesen, Tjeerd Weijers, Ronald Kortekaas and Kasper van Nieuwland for technical assistance and Michel Fruchart for valuable discussions. M.B. acknowledges funding from the European Research Council under Grant Agreement No. 101117080. C.C. and J.V. acknowledge funding from the European Research Council under Grant Agreement No. 852587 and from the Netherlands Organisation for Scientific Research (NWO) under grant agreement VI.Vidi.213.131.3. C.S. and V.V. acknowledge support from the Simons Foundation, the Complex Dynamics and Systems Program of the Army Research Office under grant W911NF-19-1-0268, and the University of Chicago Materials Research Science and Engineering Center, which is funded by the National Science Foundation under Award No. DMR-2011854. C.S. acknowledges funding from the National Science Foundation Graduate Research Fellowship under Grant No. 1746045. JB acknowledges funding from the European Union's Horizon research and in-

novation programme under the Marie Skłodowska-Curie Grant Agreement No. 101106500.

Author contributions.
J.V., C.S., M.B., V.V. and C.C. designed the research. M.B., J.V. and C.C. designed the experiments, J.V. and M.B. and performed the measurements. M.B., C. S. and J.V. analysed results. J.V. and C.S. performed the numerical simulations and optimisation. J.V, C.S., J.B., A.S. and V.V. carried out the theoretical calculations. All authors contributed to the interpretation of the data. J.V., C.S., V.V. and C.C. wrote the paper with the input from all authors.

Code and data availability.
The data and analysis codes are available at https://doi.org/10.5281/zenodo.13844137

Supplementary Information.
Supplementary Information is available for this paper.

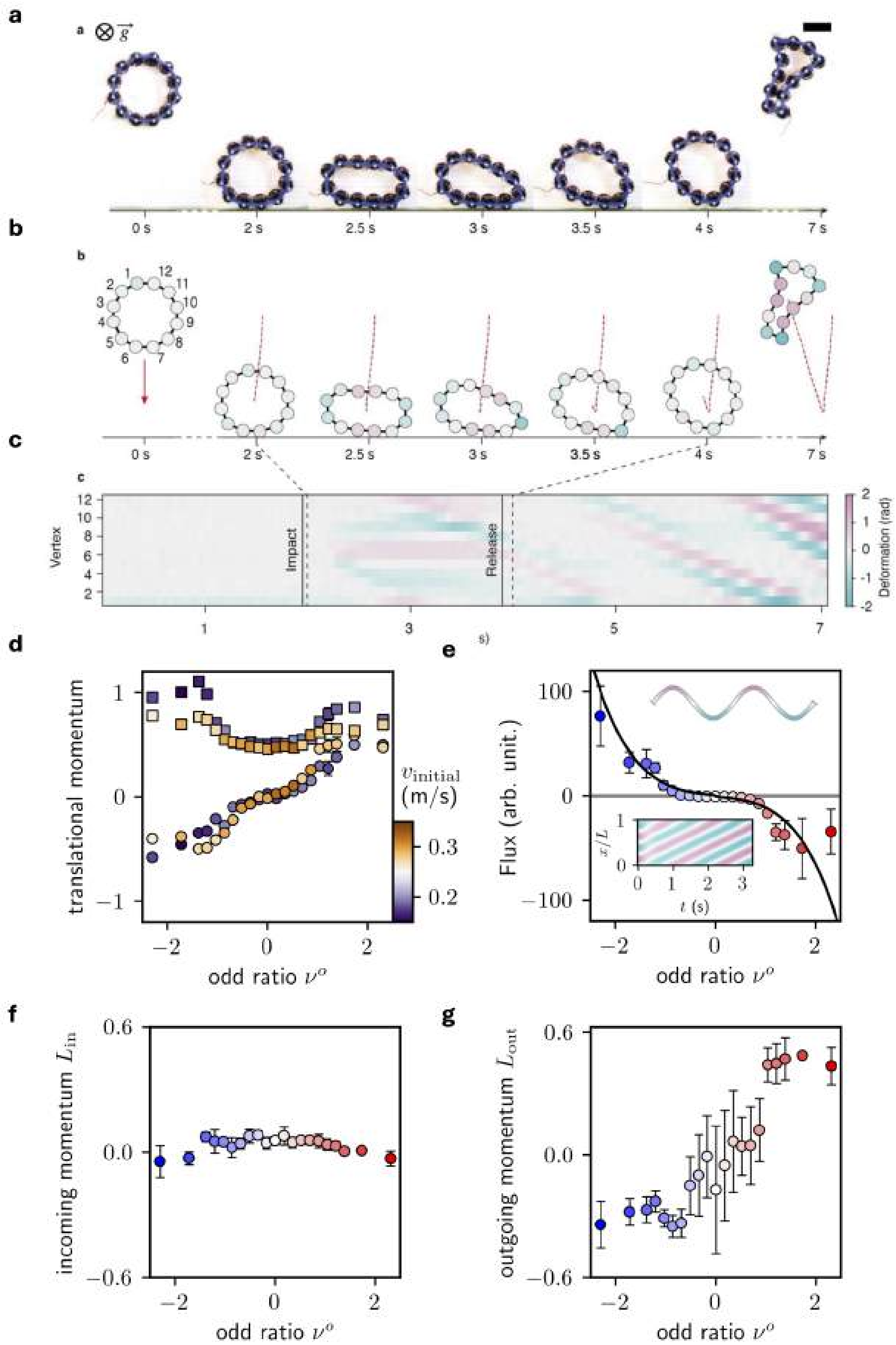

Extended Data FIG. 1. **Non-Hermitian skin effect and transient dynamics in the 12-vertex ring upon impact. (a)** The active projectile with $\nu^o < 0$ is vertically incident against a wall. **(b-c)** The angular deformation of each vertex is plotted as a function of time, revealing a unidirectional wave propagating in the opposite direction of Fig. 2a. See also Supplemental Video 2. **(d)** The ratio between incoming and outgoing momenta $p_{\text{out}}/p_{\text{in}}$ in the x- (round markers) and y-directions (square markers) as a function of odd ratio ν^o for an initial velocity v_{in} of 0.26 m/s (blue) and 0.34 m/s (orange). The data of Fig 2c is found by averaging over these two initial conditions. **(e)** Inset, top: The chain is modelled as a continuous ring (see S.I. section S1). Inset, bottom: We evolve Eq. (M12) on a 1D periodic ring using the second harmonic as an initial condition. Color indicates deviation in curvature. Main: the flux $\Psi = \dot{\theta} e^{\dot{A} t_c / A}$ with $z = Ae^{i\theta}$ (see S.I. section S1B) quantifies the unidirectionality and amplification of the waves in experiment. Black lines show flux values calculated from solutions to Eq. (M12), calibrated with experimentally determined parameters for the ring described in the Methods. Note that in the regime $|\kappa^a|/\kappa > 0.45$ there are large error bars. This is most likely due to the fact that the ring sits in the unstable regime described in Fig. 4a-d, where deformations are large. Note also that we see relatively good agreement with the prediction based on Eq. (M12) in spite of the fact that this model assumes small deflection about flat geometry. **(f,g)** Angular momentum of the odd ring before and after impact. The ring is launched with no angular momentum, but odd response imparts rotational momentum which scales with the odd stiffness κ^a. Angular momenta are normalised by the scale Rv_{in}, where R is the radius of the ring, and v_{in} is the incoming velocity.

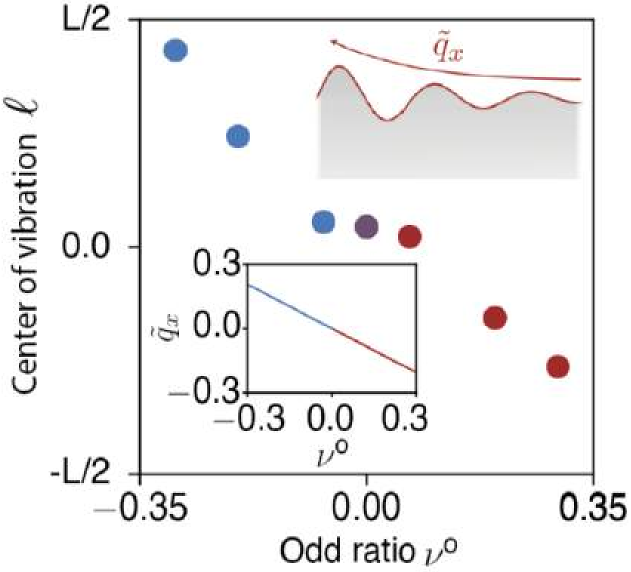

Extended Data FIG. 2. **Unidirectional Rayleigh waves**. The center of vibration ℓ [see Eq. (M24)] measured as a function of the odd ratio ν^o. (Inset top right) The continuum model analyzed in S.I. section S1A implies the existence of Rayleigh waves whose vibrational modes grow exponentially along the surface with inverse decay length q_x, see S.I. section S1. (Inset bottom left) We plot $\tilde{q}_x = q_x\sqrt{\frac{E}{\rho\omega^2}}$ as a function of the odd ratio ν^o predicted by the continuum theory, where ω is the frequency of the wave, and E and ρ are the Young's modulus and density of the wall.

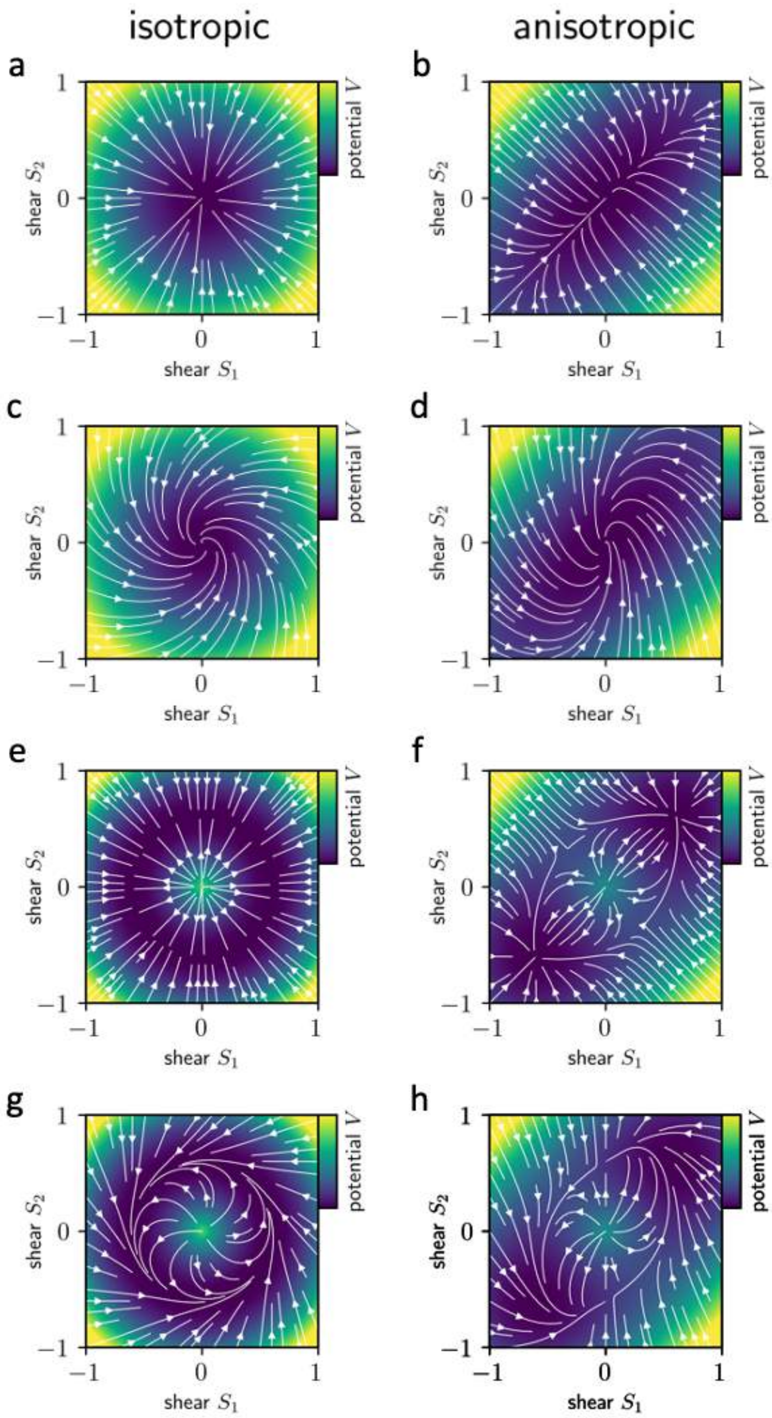

Extended Data FIG. 3. **The effect of anisotropy on odd elastic work cycles.** Symmetric couplings between the two shear modes S_1 and S_2 can only arise in elastic solids with broken isotropy. The shear modes of an anisotropic odd elastic solid would evolve according to following equation of motion: $\ddot{z} = -z + i\nu^o z + i\nu^e z^* - \Gamma z$, where z^* is the complex conjugate of $z = S_1 + iS_2$ and ν^e parametrises the symmetric coupling and thus the measure of anisotropy. The simple quadratic potential of a passive elastic solid with $\nu^o = \nu^e = 0$ **(a)** attains an anisotropy axis when ν^e becomes nonzero **(b)**. An odd elastic solid with $\nu^o \neq 0$ and $\nu^e = 0$ features a curled force field that does not derive from its potential but is still isotropic, evidenced by the rotational symmetry of the forcefield **(c)**. When the symmetric coupling is turned on and $\nu^e \neq 0$, the anisotropic odd solid will have a different response depending on the direction of an applied shear strain **(d)**. While the linear, nonreciprocal constitutive relationship in Eq. (4) requires activity, asymmetric deflection can also occur in passive anisotropic or chiral media, or those which are nonreciprocal via nonlinearities [65, 66]. **(e-h)** Gravity and normal forces arising from the treadmill introduce an extra nonlinear term $z/|z|$. A passive isotropic solid ($\nu^o = \nu^e = 0$) placed in this setting will be attracted to one of the shear configuration on the ring of fixed points **(e)**. For a passive anisotropic solid ($\nu^e \neq 0$) such as a rugbyball, not all orientations are equipotential and only two fixed points remain **(f)**. Anisotropy modifies the limit cycle exhibited by an odd elastic solid from a circular trajectory **(g)** to a more elliptically shaped trajectory **(h)**.

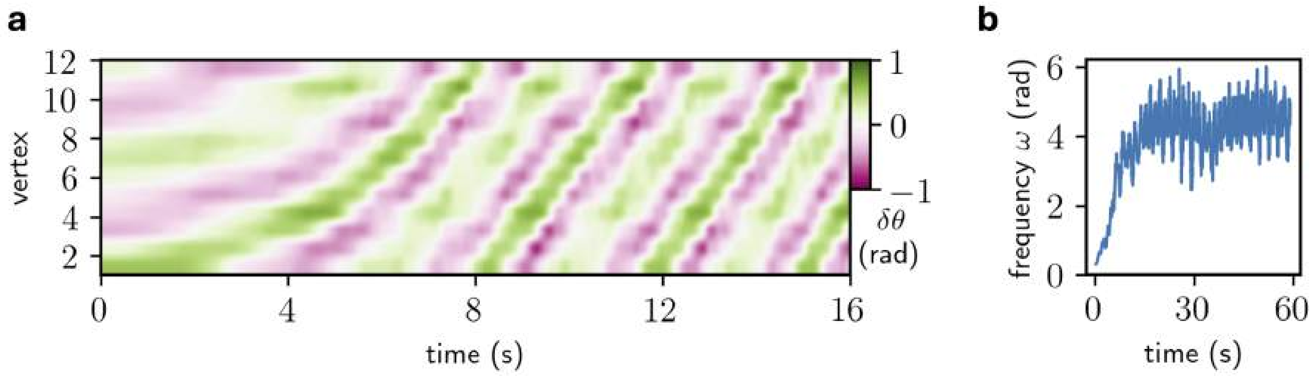

Extended Data FIG. 4. **A cycle of shape changes of increasing frequency drives adaptive locomotion.** **(a)** A kymograph of the internal deformations $\delta\theta_i$ of the locomoting ring of Fig. 2d during acceleration from a static initial condition. **(b)** Cycling frequency of the locomoting ring during the acceleration phase.

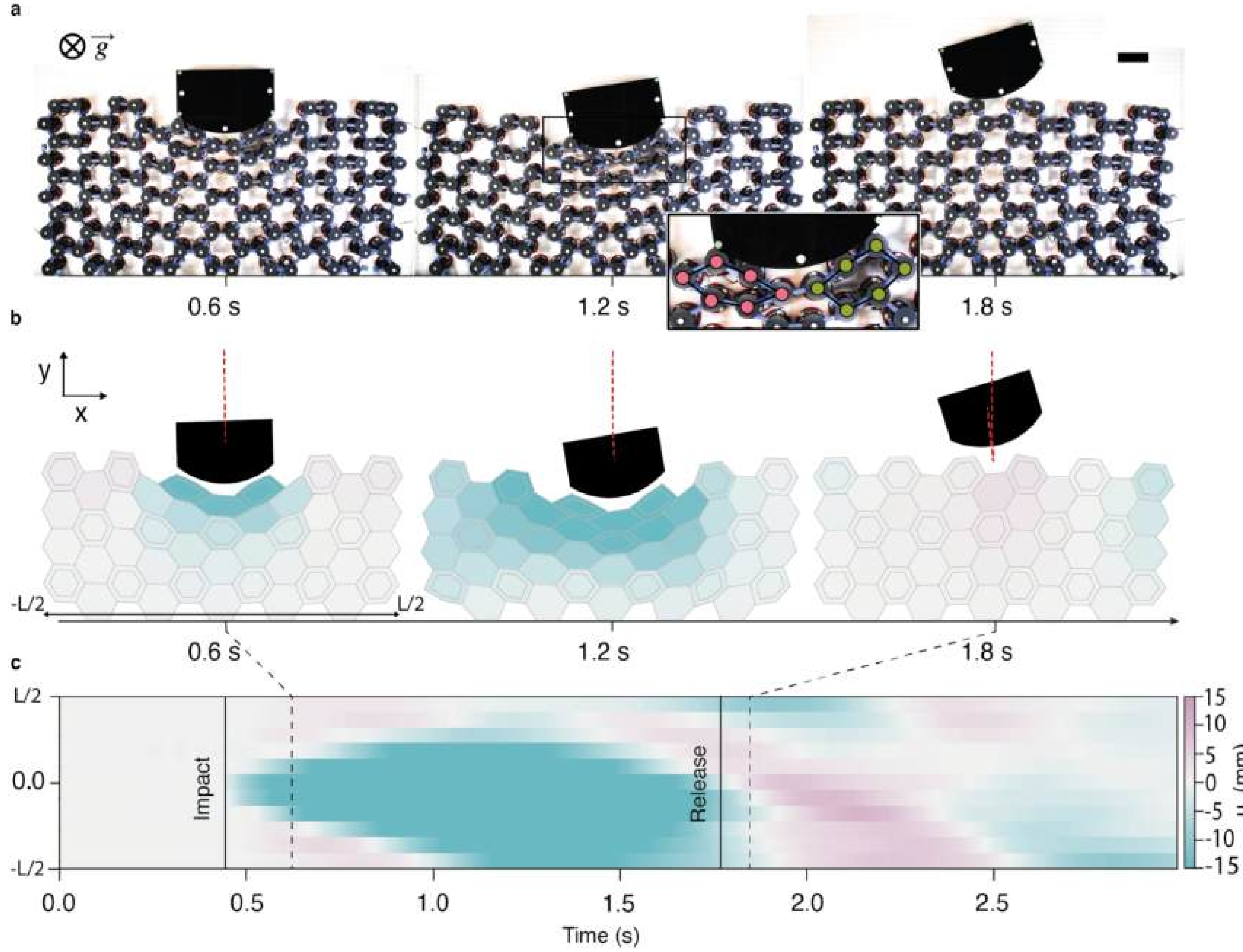

Extended Data FIG. 5. **(a)** A passive projectile is launched at the active wall of Fig.1i with $\kappa^a < 0$. **(b)** Corresponding reconstructions of the wall, where the vertical displacement u_y of each hexagon is plotted. **(c)** The displacement is averaged over each column u_y and is shown as a function of time and of the horizontal coordinate x.

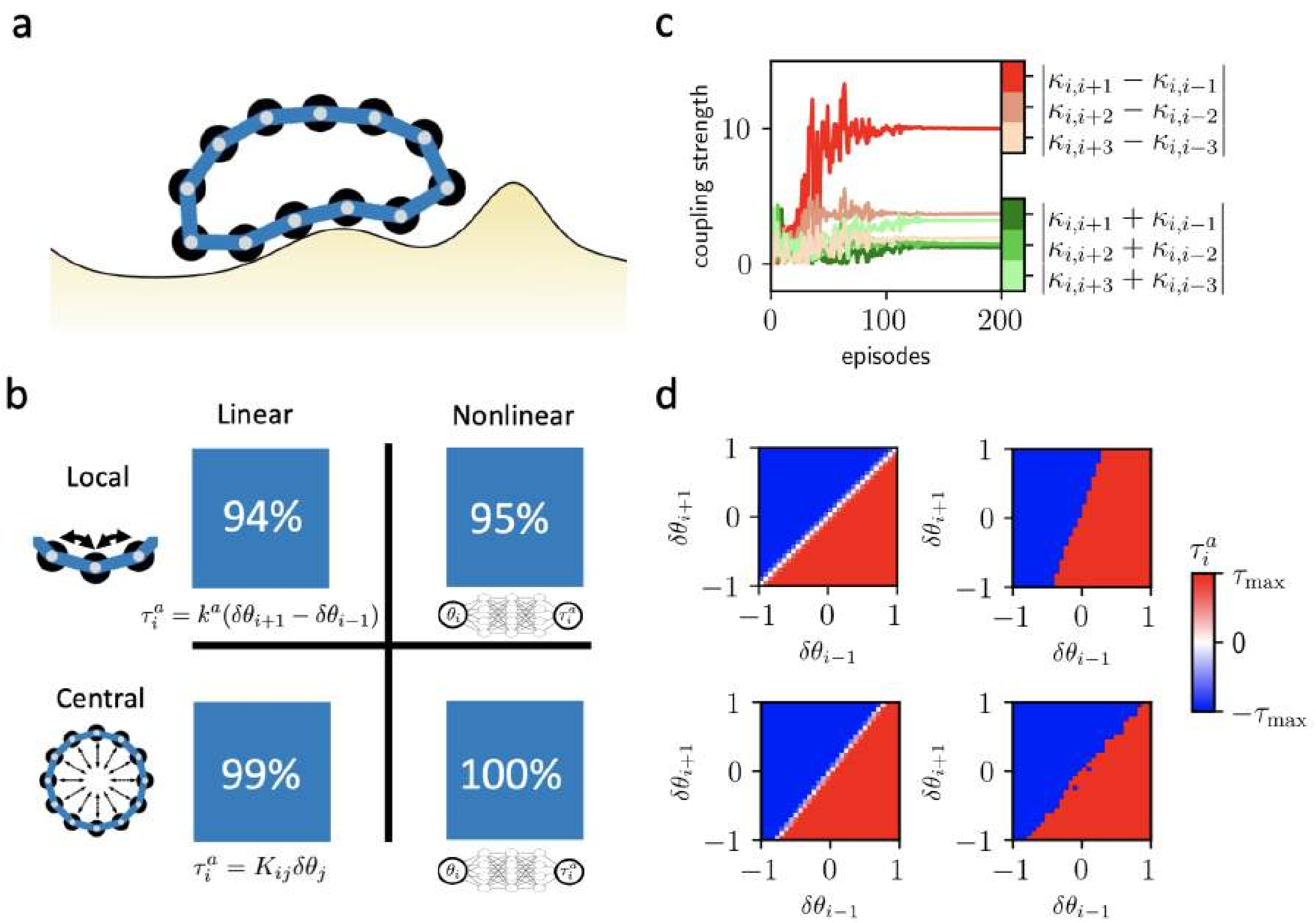

Extended Data FIG. 6. **Benchmark of locomotion performance in a 12-vertex ring.** **(a)** A snapshot of simulation of the active solid locomoting on complex terrain generated from a sum of random Gaussian functions (see S.I. section S4). **(b)** A benchmark of the locomotion performance of the local and linear control scheme (top left) using angle information from neighboring vertices $\delta\theta_{i\pm1}$ to actuate a torque as discussed in the Main text. We optimise the longrange interaction strengths given by the dynamical matrix K_{ij} of a centralised control scheme (bottom left), and the weights and biases of multilayer perceptron with access to local (top right) and centralised angle information (top right). **(c)** Evolution of the symmetric (shades of green) and antisymmetric (shades of red) longrange coupling strengths during optimization. **(d)** The optimised actuation torque τ_i as a function of neighboring angles $\delta\theta_{i\pm1}$ for local feedback (top left) and the local network (top right). For central control (bottom), we find the average output torque τ_i over a set of randomised remaining entries of the angle input vector.